Preprint – This is a non-peer-reviewed manuscript submitted to EarthArXiv

Hamiltonian Monte Carlo applied to inverse petrological problems

Dimitrios Moutzouris, Annalena Stroh, Simon Schorn, and Evangelos Moulas

Institute of Geosciences and Mainz Institute of Multiscale Modeling (M^3ODEL), Johannes Gutenberg University, Mainz, Germany

March 2, 2026

Abstract

Inversion is inherent in petrology and is used to investigate both experimental and natural field data. When field observations, petrography, geochronology, and geochemistry are combined with numerical models, inversion is used to quantify important parameters that provide insights into natural processes involved in the petrogenesis of rocks. Additionally, with the current advances in the field of petrology, a large number of parameters can be explored. However, an increase in the number of parameters also raises the overall computational cost. Therefore, appropriate algorithms are needed to efficiently explore such high-dimensional parameter spaces. In this contribution, we demonstrate the use of Hamiltonian Monte Carlo for inverse diffusion modeling within a petrological framework. We begin by describing the theoretical background of the approach. We show that Hamiltonian Monte Carlo is a powerful tool to explore high-dimensional parameter spaces and therefore quantify the uncertainties of key parameters in petrological forward models. By using compositional garnet data and geochronological $^{40}Ar/^{39}Ar$ muscovite data from the Pindos metamorphic sole as an example, we invert for the initial cooling rate, initial equilibration temperature, and the effective grain size of the investigated minerals. A key finding in our work is the strong agreement between inverse garnet diffusion modeling and Ar diffusion in muscovite, even though the two approaches are entirely independent. Our joint approach shows that an initial equilibration temperature of 637.6 ± 8.3 °C and an initial cooling rate of 241.3 ± 76.5 °C Myr^{-1} are required to explain not only previous thermobarometric and geochronological data but also the major-element zonation of garnets and the $^{40}Ar/^{39}Ar$ age of muscovite from the Pindos metamorphic sole. Moreover, our inversion shows that the effective grain size of muscovite plays a negligible role in fitting the observed $^{40}Ar/^{39}Ar$ age of the mineral. The calculated cooling rates and the preservation of high equilibration temperatures, garnet zonation, and residual quartz-in-garnet pressures strongly support shear heating as the primary mechanism for the formation of the Pindos metamorphic sole.

Corresponding author:
dmoutzou@uni-mainz.de

1 Introduction

Igneous and metamorphic rocks represent the final state of complex physical and chemical processes, recording integrated pressure–temperature–time (P–T–t) histories. Throughout their evolution, rocks undergo coupled textural, mineralogical, mechanical, and compositional changes that collectively encode the processes operating during their formation and subsequent modification. Since the advancement of analytical and computational techniques, the evolution of rocks can be quantified with the use of thermodynamic and numerical models. As an example, inverse diffusion models have been widely applied to reproduce the compositional profiles of minerals in a diverse range of systems, spanning from meteorites to magmatic and metamorphic rocks (e.g., Costa et al., 2020; Kent et al., 2001; Medaris et al., 1990; Olker et al., 2003). For rocks that (re)crystallize at elevated temperatures, mineral compositional profiles evolve in a time-dependent manner as a result of active intracrystalline diffusion. As temperatures decrease toward near-surface conditions, chemical diffusivities in most silicate minerals become negligibly small (e.g., Zhang, 2010). Consequently, the compositional profiles preserved in minerals effectively record the duration of high-temperature geological processes and can be used to quantify and constrain their timescales (Faryad & Chakraborty, 2005; Lasaga, 1983; Schorn et al., 2024; Schwarzenbach et al., 2021). Interpreting such profiles therefore constitutes an inverse problem, in which observed present-day compositions are used to reconstruct the underlying thermal and temporal evolution (e.g., Engl et al., 1996). Alternatively to the temporal estimates, numerical diffusion models can be used to quantify key parameters such as the effective cooling rate (e.g., Burg & Moulas, 2022; Lasaga et al., 1977; Spear, 2004). The estimated cooling rates may be used to understand the geodynamic processes involved in the evolution of a rock. Whether time spent at high temperatures or effective cooling rate is estimated, the main objective of inverse diffusion modelling is to quantify petrologically useful parameters that best reproduce the observed natural data while satisfying given constraints (e.g., estimated P-T conditions) and physical models.

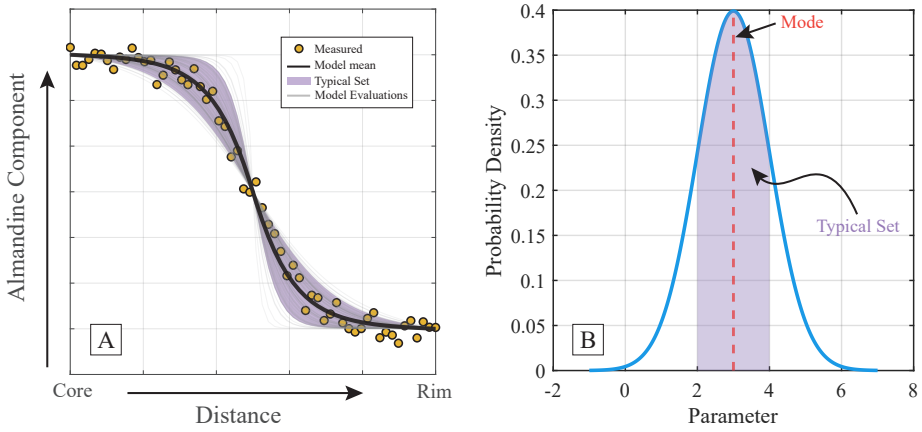

Figure 1: Conceptual illustration highlighting the primary goal of inverse diffusion modelling in garnet (almandine component). (A) A large number of models (grey lines) is evaluated using different values of a physical parameter, such as cooling rate. Only some of these models successfully reproduce the observed compositional data (for example, the almandine profile from core to rim) within their uncertainty. The parameter values associated with these successful models form the typical set. That is the range of parameter values that is the most consistent with the data. (B) This invertible parameter can be represented by a probability distribution, such as a normal (Gaussian) distribution. In this distribution, the typical set corresponds to the high-probability region with the highest probability of reproducing the observations. The single value with the highest probability is the mode. The primary objective of inversion is to identify and quantify this typical set of parameter values.

Petrological inversion becomes more complex in the absence of well-defined constraints. For instance, in the context of diffusion modeling, if the initial peak metamorphic conditions are un-

known, infinite combinations of initial temperature and cooling rate yield indistinguishable good fits to the observed compositional data. The implication of this is that as many combinations result in the identical compositional profile preserved in compositionally zoned minerals. In fact, the choice of constraining the timescale (also known as diffusion chronometry) or the cooling rate (diffusion geospeedometry) from the same compositional data testifies to the fact that different thermal histories may yield equally satisfying results. This lack of uniqueness makes inverse diffusion-type models ill-posed by definition (e.g., Kabanikhin, 2008).

Another source of uncertainty in inversion modelling stems from the inherent susceptibility of petrological data to analytical and random errors, commonly related to measurement methodologies such as electron microprobe analysis (EPMA; e.g., Batanova et al., 2018). This means that repeated measurements will inevitably yield different observations. Therefore, a range of models may be considered as consistent (within error) with the observed data (Figure 1A). Consequently, the inverted parameters derived from this set of models also inherit uncertainties reflecting the variability of the data (Figure 1B). Various approaches exist to quantify the uncertainty of the invertible parameters, each showing distinct advantages and limitations.

An important aspect of inversion is the number of parameters involved. In simple cases with one to two variable parameters, a direct search algorithm that scans the full parameter range can adequately explore the parameter space with reasonable computational cost (e.g., Burg & Moulas, 2022). As numerical models continue to develop and incorporate greater physical complexity, the number of parameters that can be explored through inversion drastically increases (e.g., Mackay-Champion & Cawood, 2025). This leads to a substantial rise in computational cost. Consequently, more advanced algorithms are required to efficiently explore high-dimensional parameter spaces and at the same time enable rigorous quantification of the associated uncertainties.

Here we apply the Hamiltonian Monte Carlo (HMC) method to inverse diffusion petrological/geochemical modeling to explore the parameter space and quantify uncertainties of critical parameters such as the cooling rate, the initial equilibration temperature and the effective mineral grain size in the case of muscovite Ar diffusion. Unlike other sampling techniques, HMC is a gradient-based method that offers significant advantages particularly in its ability to efficiently handle high-dimensional parameter spaces. To test HMC, we used petrological data from the metamorphic sole rocks of the Pindos ophiolite in northwestern Greece (Moutzouris et al., 2025). These rocks are well-suited for this method due to the relative simplicity of their P-T evolution and the consistency of results. Our previous findings show that the rocks underwent rapid cooling under relatively high temperatures (Moutzouris et al., 2025). The joint inversion presented in this paper utilizes two different forward problems of petrological interest. The first forward problem is the diffusion of major elements in garnet and the second is the diffusion of radiogenic argon in muscovite. The incorporation of the data relevant to two different petrological datasets -garnet and muscovite- suggests that both datasets can be explained if the sole rocks experienced very high values of initial (and transient) cooling rates (241.3 ± 76.5 °C/Myr). The latter results are in agreement with a geodynamic scenario that requires the fast tectonic movement of the sole rocks with contributions from shear heating (Tagliaferri et al., 2025). Our results show that the integration of multiple independent physical models in combination with petrological constraints and rigorous uncertainty quantification provides improved insights into the geodynamic processes involved.

2 Hamiltonian Monte Carlo

The HMC algorithm is a variant of the Markov Chain Monte Carlo (MCMC) class of algorithms. MCMC originates from the pioneering work of Metropolis et al. (1953), who used it to study equations of state of interacting molecules. HMC, initially termed Hybrid Monte Carlo, was first introduced by Duane et al. (1987) in the context of molecular dynamics simulations. Since then, and aided by advances in computational power, HMC has been successfully applied to a wide range of statistical and physical problems (e.g., Hajian, 2007; Mehlig et al., 1992; Neal, 1996). Within the geosciences, Sen & Biswas (2017) were amongst the first to apply HMC to seismic inversion. A comparative study by Reuber (2021), along with the contributions of Fichtner & Zunino (2019) and Fichtner et al. (2021), have demonstrated the potential of HMC methods for

addressing geoscientific inversion-type problems. Since then, HMC has been predominantly employed in geophysical inversion (e.g., De Lima et al., 2024; Gebraad et al., 2020; Koch et al., 2020; Y. Xu et al., 2025; Zunino et al., 2022), while petrological applications are still missing. Here we aim at addressing this shortcoming by first outlining the fundamental concepts underlying HMC, followed by a practical petrological application to the Pindos metamorphic sole (northern Greece; Moutzouris et al., 2025) showcasing the capabilities of this method. Finally, we conclude this contribution with some potential implications on the geodynamic evolution of the studied rocks.

Starting from petrologic observations, we can infer geodynamic processes once certain physical parameters, such as the peak temperature and the initial cooling rate, are constrained. These parameters define a space that must be explored to determine which parameter combinations provide adequate data fits. A satisfactory data fit means that the modeled output matches the observed data within their uncertainty. The region in the parameter space resulting in such fits is referred to as the typical set (Figure 1B, 2A). Within the typical set lies the mode, which corresponds to the parameter values with the highest probability of generating the observed data. For example, in a one-dimensional Gaussian distribution, the mode is located at the peak of the probability curve (Figure 1B). However, a comprehensive understanding of the parameter space requires examining not only the mode but also its surrounding neighborhood, where probabilities remain high and most of the probability mass is concentrated. A typical petrological example of such high probabilities is the numerous combinations of cooling rates and near-peak temperatures that can be used to fit the same diffusion data (Burg & Moulas, 2022; Tagliaferri et al., 2025). With increasing number of invertible parameters, the typical set exploration becomes computationally challenging and efficient algorithms are required to explore it.

The HMC method is based on the concept of Hamiltonian energy from classical mechanics (e.g., Arnold, 1974) and it is used by analogy in inverse problems. In classical mechanics, the Hamiltonian energy is used to describe the evolution of a system of particles by updating their position and momentum over time. The positions and momenta of the system's parts are also called the "canonical variables", and they define a space known as the phase space. Thus, the evolution of a mechanical system can be represented as a trajectory in phase space. The mechanical system under investigation could be something as simple as a harmonic oscillator such as a pendulum or a more complex mechanical configuration. One of the advantages of the Hamiltonian approach lies in the fact that the evolution of a physical system is described using a set of ordinary differential equations for position and momentum. Therefore, once a physical system evolves in time, its position and momentum mark a trajectory in phase space (Figure 2). If the evolution of a system is known within a certain region of the phase space, then, we have mapped out all the possible states of the mechanical system.

In inverse models having several parameters, the challenge is to efficiently sample the parameter space that contains all possible states of the system. In this regard, by "states" we define the possible sets of parameters that provide adequate fits to our dataset. By analogy to true Hamiltonian mechanics, HMC treats model parameters as position variables $(\theta_1, \theta_2, \dots)$ within the phase space, and the misfit function –which defines the goodness-of-fit between model and observable data– is treated as analogous to the potential energy $V(\theta_1, \theta_2, \dots)$. As such, minima in the misfit function correspond to the optimal set of parameters – those that lead to the best fit of the input data. Artificial momenta are then introduced instead of real physical momenta that aid to the exploration of the parameter space. Note that the usage of artificial momenta does not affect the inversion results and is only introduced to optimize the computation in a self-consistent manner. For a detailed discussion of the HMC method, the reader is referred to Neal (2011) and Betancourt (2018).

In the framework of HMC, the Hamiltonian energy is defined as the sum of a potential and a kinetic energy:

$$H(\boldsymbol{\theta}, \boldsymbol{p}) = T(\boldsymbol{p}) + V(\boldsymbol{\theta}) \tag{1}$$

where $\boldsymbol{\theta}$ represents the vector of invertible parameters of interest, $\boldsymbol{p}$ stands for the vector of the artificial momenta, $H(\boldsymbol{\theta}, \boldsymbol{p})$ is the Hamiltonian energy, $T(\boldsymbol{p})$ is the kinetic energy as a function of the momentum vector $\boldsymbol{p}$, and $V(\boldsymbol{\theta})$ is the potential energy function of the parameter vector $\boldsymbol{\theta}$. $H(\boldsymbol{\theta}, \boldsymbol{p})$ quantifies the total amount of energy of a system at given coordinates $(\boldsymbol{\theta})$ and momenta $(\boldsymbol{p})$. For an intuitive analogy, $\boldsymbol{\theta}$ can be thought of as the position of a harmonic oscillator and $\boldsymbol{p}$ as its momentum. In this paper, $\boldsymbol{\theta}$ will represent the vector of invertible parameters (e.g., cooling rate

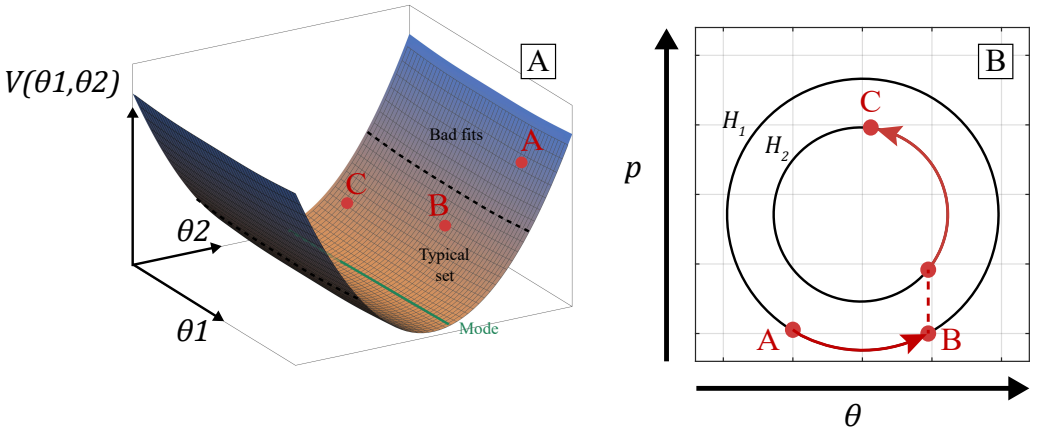

Figure 2: Simplified illustration showing the main concept of Hamiltonian Monte Carlo. (A) Schematic plot showing the misfit function $V(\theta_1, \theta_2)$, which in this case defines a valley for two invertible parameters θ_1 and θ_2. The slopes of the valley correspond to bad fits between model and data. The valley floor represents the mode of this two-dimensional space. The main goal of Hamiltonian Monte Carlo is to propose new samples that possibly start from the slopes but eventually explore the typical set. This corresponds to going from point A to points B and C (see main text for more details). (B) The exploration is achieved by updating the parameters ($\boldsymbol{\theta}$) and their corresponding momenta ($\boldsymbol{p}$) along trajectories of constant Hamiltonian energy (H_1, H_2).

and initial equilibration temperature) and $\boldsymbol{p}$ their corresponding artificial momenta. The motion of a Hamiltonian system can be calculated with the canonical equations defined as:

$$\frac{d\theta_i}{dt} = \frac{\partial H(\boldsymbol{\theta}, \boldsymbol{p})}{\partial p_i} \tag{2}$$

$$\frac{dp_i}{dt} = -\frac{\partial H(\boldsymbol{\theta}, \boldsymbol{p})}{\partial \theta_i} \tag{3}$$

where t represents an arbitrary/artificial time and i represents the index of each invertible parameter and its corresponding momentum. Note that each θ_i has its own unique p_i. This means that for a system of two parameters, the total problem is four-dimensional.

Equations (2) and (3) constitute a set of coupled ordinary differential equations that are used to update the parameters and momenta. The nature of these equations and their implying properties constitute the main tool that allows the algorithm to explore the typical set (Figure 2). Since we are not considering a true mechanical system but an analogous one, this exploration requires appropriate definitions of the potential and kinetic energy of the system. The potential energy of the system may be formulated as a misfit function (e.g., Fichtner et al., 2021):

$$V(\boldsymbol{\theta}) = J = \frac{1}{2}\left(\mathbf{F}_{\boldsymbol{\theta}}^{\text{mod}} - \mathbf{F}^{\text{obs}}\right)^T \left(\mathbf{F}_{\boldsymbol{\theta}}^{\text{mod}} - \mathbf{F}^{\text{obs}}\right) \tag{4}$$

where $\mathbf{F}^{\text{obs}}$ represents the observed natural data at n locations (e.g., EPMA data along a 1D mineral zoning profile), and $\mathbf{F}_{\boldsymbol{\theta}}^{\text{mod}}$ represents the modeled compositions at the same locations. The scaled misfit J is non-negative as in a typical least-squares approach. A large value of J, and therefore $V(\boldsymbol{\theta})$, means that the model does not reproduce the observed data in a satisfactory way. Thus, in the framework of inversion, the smaller the "potential energy", the better the fit.

The kinetic energy is traditionally introduced as:

$$T(\boldsymbol{p}) = \frac{1}{2}\boldsymbol{p}^T \mathbf{M}^{-1} \boldsymbol{p} \tag{5}$$

where $\mathbf{M}$ represents a symmetric and positive-definite matrix, the superscript "T" represents the transpose of the vector $\boldsymbol{p}$, and the superscript "-1" denotes the inverse of the matrix $\mathbf{M}$. This formulation is analogous to the general kinetic energy expression used in classical mechanics, $\frac{1}{2}mp^2$,

where m is the mass of a particle and p is its momentum. However, more complicated formulations of kinetic energy (e.g., the Riemannian approach) may also be used depending on the application and for efficiency reasons (e.g., Girolami & Calderhead, 2011). The mass matrix $\mathbf{M}$ could either represent a diagonal variance matrix that applies specific weights to different momenta, or a covariance matrix that also considers correlations between the different momenta. The mass matrix is commonly assumed to be equal to the unit matrix. However, $\mathbf{M}$ is critically used to guide efficient exploration (e.g., Fichtner et al., 2021).

With the current definitions of potential and kinetic energy, the Hamiltonian energy takes the following form:

$$H(\boldsymbol{\theta}, \boldsymbol{p}) = \frac{1}{2}\boldsymbol{p}^T\mathbf{M}^{-1}\boldsymbol{p} + J \tag{6}$$

and therefore, the canonical equations become:

$$\frac{d\theta_i}{dt} = \frac{\partial H(\boldsymbol{\theta}, \boldsymbol{p})}{\partial p_i} = \left[\mathbf{M}^{-1}\boldsymbol{p}\right]_i \tag{7}$$

$$\frac{dp_i}{dt} = -\frac{\partial H(\boldsymbol{\theta}, \boldsymbol{p})}{\partial \theta_i} = -\frac{dV(\boldsymbol{\theta})}{d\theta_i} = -\frac{dJ}{d\theta_i} \tag{8}$$

Equations (7) and (8) are solved numerically to update the positions (i.e., the invertible parameters) and (artificial) momenta of the system. Notice that based on Equation (7), the parameter update is dependent on the momentum. Inversely, the momentum update is dependent on the parameters according to Equation (8). In this way, the two variables form a feedback loop with one influencing the other.

To gain more insights into the dynamics, suppose the potential energy valley depicted in Figure 2A is defined by two invertible parameters θ_1 and θ_2 such as cooling rate and initial temperature. Areas that are high at the slopes of the valley correspond to high misfits and therefore bad fits between model outputs and data. The valley floor defines the best fits. The mode is the set of lower-most points that correspond to the minimum potential energy. Moreover, the typical set is the region around the mode that contains models that have high probability of reproducing the data.

Standard HMC algorithms begin by sampling random momenta from a Gaussian distribution $\mathcal{N}(\mathbf{0}, \mathbf{M})$. This means that all momenta are drawn in a stochastic (random) way with a mean value of 0 and they can be correlated or scaled based on the mass matrix $\mathbf{M}$. An initial guess is also made for the invertible parameters θ_1 and θ_2. The initial draw of parameters positions the algorithm at a point, such as point A in Figure 2A. This point has a high potential energy (i.e., a relatively bad data fit). Since it exists outside of the typical set, we use the canonical equations to propose a new acceptable sample which falls inside the typical set. For this, the canonical equations (7) and (8) are solved for several artificial time steps simulating a specific trajectory (for example, from point A to point B in Figure 2B). This trajectory is uniquely determined by the initial guesses of momenta and parameters and the solution of the canonical equations. By simulating a trajectory, we make a large jump from point A to a new point B on Figure 2B. Crucially, along this trajectory, the Hamiltonian energy is conserved (for more details see Appendix A), while the kinetic and potential energy oscillate in magnitude so that the total energy is kept constant. This energy oscillation means that we explore different potential energy (misfit) magnitudes inside the typical set, while being confined within the typical set since the gradient of the potential energy is used.

Going from point A to point B (e.g., Figure 2), the gradient of potential energy of Equation (8) is driving the initially drawn momenta in the direction of the mode. This part of HMC is similar to gradient descent. However, we do not apply gradient descent directly on the invertible parameters (θ_1, θ_2), because this would lead to a dissipative behavior and eventually bring us directly to the mode. This would cause the algorithm to converge at the mode without being able to explore the typical set. In contrast, in the case of HMC, we are only updating the artificial momenta (i.e., the driving forces) according to the gradient of the potential energy, which is given by the misfit function defining the goodness-of-fit. Therefore, we are indirectly affecting the parameters with Equation (7), which sees the contribution of the momenta. The feedback between momentum and parameters along with the conservation of Hamiltonian energy produces non-local, oscillatory movements. After reaching point B, we continue by resampling new momenta in a random manner.

This marks the start of a new trajectory at a different Hamiltonian energy level which is still constrained within the typical set. The uncertainty in the observed data bounds the typical set as HMC progressively explores the parameter space. At point B, an accept/reject step is applied to ensure correct numerical implementation (see Appendix C for more details).

The solution of the canonical equations allows the algorithm to avoid areas of poor fit by using the gradient of the potential energy. Simultaneously, this avoids stagnation at the mode. To demonstrate this point, suppose that the combination of parameters reaches the mode at the misfit-valley floor. At this point, the gradient of the misfit function w.r.t. the parameters is $\frac{dJ}{d\theta_i} = 0$. The consequence of this is that the time derivative of the momenta is $\frac{dp_i}{dt} = 0$ and therefore the momentum remains constant (i.e., time invariant). However, the time derivative of the parameters is $\frac{d\theta_i}{dt} = \left[\mathbf{M}^{-1}\boldsymbol{p}\right]_i$, and since, in this case, the momenta are constant yet non-zero, the parameters will still be updated. In fact, the only way to converge at the mode is if the momentum $\boldsymbol{p} = \mathbf{0}$. However, the random sampling of momenta makes this scenario almost impossible, as desired in order to sample the typical set.

The previous parts describe the main logic of Hamiltonian Monte Carlo. However, most published algorithms that perform HMC, such as Stan (Carpenter et al., 2017) and AdvancedHMC.jl (Fjelde et al., 2025; Ge et al., 2018; Xu et al., 2020), use a different but equivalent approach. These algorithms define the Hamiltonian energy in the following manner:

$$H(\boldsymbol{\theta}, \boldsymbol{p}) = \frac{1}{2}\boldsymbol{p}^T\mathbf{M}^{-1}\boldsymbol{p} - \log\left[\mathcal{L}(\mathbf{F}^{\text{obs}} \mid \boldsymbol{\theta})\,\Pi(\boldsymbol{\theta})\right] \tag{9}$$

where $\mathcal{L}(\mathbf{F}^{\text{obs}} \mid \boldsymbol{\theta})$ is called the likelihood function and $\Pi(\boldsymbol{\theta})$ is the prior probability of $\boldsymbol{\theta}$. The symbol "|" denotes that the likelihood is a conditional probability. The first term on the right-hand side is the kinetic energy $T(\boldsymbol{p})$ (Equation 5), and the second term is the potential energy $V(\boldsymbol{\theta})$. $\Pi(\boldsymbol{\theta})$ represents prior heuristic knowledge of the parameters $\boldsymbol{\theta}$. For example, $\Pi(\boldsymbol{\theta})$ may be the initial temperature assumed to follow a normal distribution with a specified mean and standard deviation (e.g., 625 ± 25 °C). This type of prior information can be derived from petrological data and other constraints like thermobarometry, or simply be assumed and tested. Note that $\Pi(\boldsymbol{\theta})$ is a constant distribution and does not evolve during the simulation. $\mathcal{L}(\mathbf{F}^{\text{obs}} \mid \boldsymbol{\theta})$ serves an equivalent purpose to the misfit function of Equation (4). It quantifies how the modeled values deviate from the observed data for a given set of $\boldsymbol{\theta}$. In other words, it expresses how probable it is to obtain $\mathbf{F}^{\text{obs}}$, given the specified set of parameters $\boldsymbol{\theta}$. The multiplication of the prior and likelihood probabilities in the second term on the right-hand side of Equation (9) defines the unnormalized posterior probability. This is the target probability that we are aiming to obtain (e.g., Bailer-Jones, 2017). The posterior probability, usually denoted as the conditional $\Pi(\boldsymbol{\theta} \mid \mathbf{F}^{\text{obs}})$, simply expresses how the values of the parameters are distributed based on their ability to reproduce the observed data within their respective errors. Equation (9) is a direct equivalent of Equation (6). This is because the small non-negative values of $\mathcal{L}(\mathbf{F}^{\text{obs}} \mid \boldsymbol{\theta})$ correspond to a bad fit between model and observed data. In this case, the potential energy is high and reflects position A in Figure 2A. When the likelihood is significant, it means that the chosen invertible parameters $\boldsymbol{\theta}$ are able to reproduce the observed data $\mathbf{F}^{\text{obs}}$, following the Bayesian formalism. For a more detailed explanation on the analogy between the misfit formulation and the Bayesian approach, the reader is referred to Appendix B. For additional insights into the HMC algorithm, the reader is referred to Appendix C.

3 Methods

3.1 Turing.jl, AdvancedHMC.jl and Automatic Differentiation

Here we used the AdvancedHMC.jl package (Xu et al., 2020) as it is implemented in the Turing.jl probabilistic library (Fjelde et al., 2025) of the Julia programming language (Bezanson et al., 2017). AdvancedHMC.jl follows the probabilistic Bayesian approach of Equation (9). However, it offers many additional options to improve adaptability and efficiency for specific problems. For example, AdvancedHMC.jl provides different choices for the numerical implementation of the canonical equations but also for the formulation of the kinetic energy. For the purposes of this paper, we use the "No-U-Turn Sampler (NUTS)" algorithm proposed by Hoffman & Gelman

(2014) and implemented in AdvancedHMC.jl. The NUTS determines automatically an optimal trajectory length for each Hamiltonian path. We adopted the normal leapfrog numerical integration scheme (see Appendix C) and a Gaussian kinetic energy (Equation 5) with an adaptive diagonal mass matrix (see Xu et al., 2020 for more details). Finally, the computation of the gradient of the potential energy with respect to the invertible parameters $\boldsymbol{\theta}$, is calculated with Automatic Differentiation (AD). This method allows accurate derivative computation. For a comprehensive overview of AD, see Neidinger (2010). We use the ForwardDiff.jl package (Revels et al., 2016) to compute derivatives within the HMC framework.

3.2 Forward numerical modelling

The main goal of our inversion is to fit the compositional profiles of garnets and also the $^{40}Ar/^{39}Ar$ (argon-argon) age of muscovite from the metamorphic sole schists of the Pindos ophiolite (Moutzouris et al., 2025). For this, we use two different numerical models and invert for the initial cooling rate, initial temperature and effective grain size (used only for the diffusion in muscovite). These parameters correspond to the vector $\boldsymbol{\theta}$. The numerical models used are GDIFF (Moulas, 2023) and KADMOS (Moulas & Brandon, 2022). GDIFF is a one-dimensional implicit Finite Difference (FD) numerical code designed to simulate multicomponent diffusion in garnet (see Appendix D for details). Here, it is used to reproduce the compositional profiles of garnets from the Pindos metamorphic sole and invert for the apparent cooling rate and the initial equilibration temperature. KADMOS, on the other hand, is a Finite Element (FE) diffusion code that models apparent $^{40}K/^{40}Ar$ (and their associated $^{40}Ar/^{39}Ar$) age profiles in various minerals (see Appendix E). It is used to simulate the apparent cooling age of a muscovite separated from a metapelite sampled at the same locality and to invert for initial cooling rate, initial equilibration temperature and effective grain size. Both GDIFF and KADMOS were translated in the high-level Julia programming language to ensure compatibility with the HMC method and AD packages while leveraging the computational efficiency for higher model performance. The codes were benchmarked to ensure they produce results identical to those of the original versions (Figures S1 and S2).

All codes developed for this study, along with their corresponding documentation that discusses technical details and usage, are published in a permanent Zenodo repository (`https://doi.org/10.5281/zenodo.18247900`). These codes allow the results presented in this paper to be reproduced. Furthermore, they may also easily be adapted for other applications and inversion using HMC, GDIFF and KADMOS. The supplementary figures are also available in the aforementioned Zenodo repository.

3.3 Analytical techniques

1D Compositional garnet profiles were acquired at the Institute of Geosciences of the Johannes Gutenberg University of Mainz (Germany) using EPMA. The analytical details regarding the equipment and operating conditions for EPMA can be found in the supplementary material of Burg & Moulas (2022). Analytical details on the measurement of the apparent age of muscovite are given in Moutzouris et al. (2025).

3.4 The Pindos metamorphic sole

The metamorphic sole of the Pindos ophiolite will serve as a case study for inverse modeling and the application of HMC. The Pindos ophiolite is located in northwestern Greece and is Jurassic in age (Liati et al., 2004). It is comprised of a metamorphic sole that includes sheets of metasediments and metabasites. Here, we focus on garnet-mica schists and a hornblende-plagioclase amphibolite studied and described in detail in Moutzouris et al. (2025). They showed that the garnet-bearing metapelites have equilibrated at upper-amphibolite facies conditions at 630 $\pm$ 20 °C and 1.1 $\pm$ 0.2 GPa A muscovite separate from the sole metapelite gave an apparent $^{40}Ar/^{39}Ar$ cooling age of 164.16 $\pm$ 0.37 Myr (million years; Moutzouris et al., 2025; their Figure 7B). Over incremental heating steps muscovite showed a curved spectrum which is typical for diffusion processes (e.g., Kelley, 2002; Turner et al., 1966). Additionally, a hornblende separate from the sole amphibolites gave an apparent $^{40}Ar/^{39}Ar$ age of 165.5 $\pm$ 0.73 Myr. Hornblende showed a well-defined apparent

age plateau indicating no argon loss. This served as a strong indication that the observed age corresponds to the formation age of the amphibolite (Moutzouris et al., 2025). Based on these data, Moutzouris et al. (2025) proposed that the rocks have cooled rapidly after the attainment of the equilibration conditions. However, the precise assessment of the cooling rates and their uncertainties was beyond the scope of the previous study.

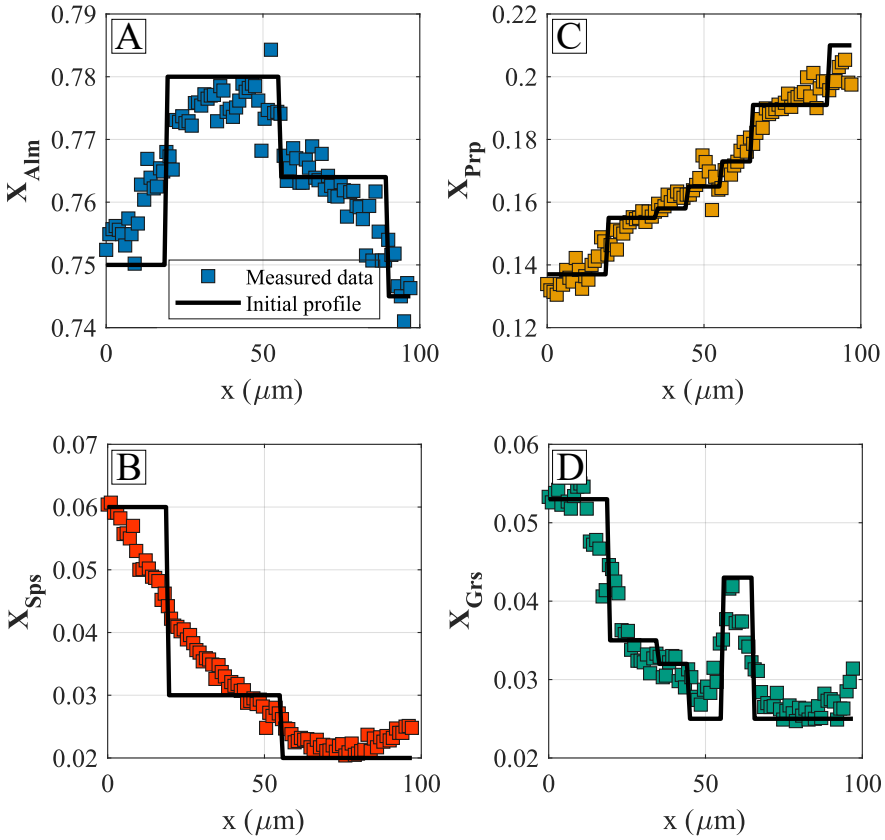

Figure 3: Measured compositional profiles of the almandine, pyrope, spessartine, and grossular components ($\mathbf{X}_{\mathrm{Alm}}$, $\mathbf{X}_{\mathrm{Prp}}$, $\mathbf{X}_{\mathrm{Sps}}$, $\mathbf{X}_{\mathrm{Grs}}$) in Grt14 and the initial conditions used for the evaluation of GDIFF models. A coordinate of 0 corresponds to the core of garnet.

4 Results

4.1 Garnet compositional profiles

Almandine-rich, porphyroblastic garnets in metapelites from the Pindos metamorphic sole exhibit strong compositional zonation. In the present study, we investigated three representative garnet porphyroblasts (Grt7, Grt14, Grt15 of Moutzouris et al., 2025), all of which display consistent zonation patterns. The garnets show a spherical geometry and they are commonly adjacent to chlorite replacing biotite (Moutzouris et al., 2025). Their radius varies from 50 to 200 μm. Figure 3 shows the compositional profile of Grt14, while the profiles of the remaining two garnets are available in the supplementary material (Figures S3 and S4). From core to rim, the almandine content increases progressively, followed by a gradual decrease toward the rim (Figure 3A). The spessartine component displays a bell-shaped zonation pattern with a slight increase in the outermost ~ 20 μm of the rim (Figure 3B). This late-stage enrichment in spessartine is typically associated with resorption processes (Kohn & Spear, 2000). The garnets show a near-linear increase in pyrope content, rising from approximately 0.13 to 0.21 (Figure 3C). In contrast, the grossular component exhibits a more complex behavior and sharp compositional profiles (Figure

3D). It is initially higher at the core (~ 0.055), followed by a gradual asymptotic decrease over the next ~ 50 μm. This is interrupted by a sharp increase to ~ 0.04 and a second smaller increase in the final ~ 10 μm toward the rim.

4.2 GDIFF: Inversion with two parameters

The compositional garnet profiles from the Pindos schists were simulated using GDIFF. Stepwise initial conditions were assumed by setting the spessartine endmember of garnet as dependent component. The initial conditions for the three different modeled garnets are shown in Figures 3, S3 and S4. We assumed a Dirichlet boundary condition (i.e., constant concentration) for the outer rim of garnets to simulate the effect of the main matrix of the rock. Moreover, we considered a no-flux Neumann boundary condition for the core of garnets due to symmetry. The tracer diffusivity coefficients of Chakraborty & Ganguly (1992) and the diffusivity matrix formulation of Lasaga (1979) were adopted. This dataset was selected as it more accurately reproduces natural data (Cheng et al., 2020).

Our investigation focused on deducing cooling rates associated with near-peak temperature conditions. Therefore, we primarily aimed to reproduce the compositional zonation formed prior to the development of the outermost garnet rim. This approach allows us to constrain the maximum cooling rate required to preserve the chemical zonation close to peak P-T conditions. We assume that the rock has followed an asymptotic cooling path of the following form (e.g., Lasaga, 1983, his Equation 17):

$$T = \frac{T_{\max}}{1 + \frac{s \cdot t}{T_{\max}}} \tag{10}$$

where $T_{\max}$ is the initial (peak) temperature, s is the initial cooling rate, and t is time in million years (Myr). $T_{\max}$ and s are the primary parameters that we invert for here. The simulations are terminated at a final temperature of 300 °C, which falls well below the closure temperature of this system, below which diffusional modification becomes negligible.

Inversion was initially carried out using a direct search approach to explore the parameter space. We assumed that $T_{\max}$ varies from 500 to 700 °C and that s varies from 50 to 500 °C/Myr, in accordance with the expected cooling rates of Moutzouris et al. (2025). . The model pressure was set to 1.1 GPa, consistent with the estimated pressure at the thermal maximum for the Pindos sole (Moutzouris et al., 2025). Direct search considers all possible combinations of the two parameters in the specified range and evaluates a unique model for each combination. The two variables are discretized with a resolution of 100 grid points per parameter. Therefore, a total of 10,000 model evaluations are required to explore the parameter space. This resolution was chosen to ensure that possible low-misfit regions are adequately resolved. In addition, the direct search approach allows the identification of local minima, if present.

Table 1: Comparison of computation time and total number of model evaluations between the direct search approach and HMC. All computations were performed using a desktop computer with an AMD Ryzen 9 7900X 12-Core processor and 64 GB of RAM.

Numerical Model	Considered Minerals	Number of Parameters	Type of Sampler	Computation Time (hours)	Model Evaluations	Number of HMC Samples
GDIFF	Grt7, Grt14 and Grt15	2	Direct Search	3.96	30,000	-
GDIFF	Grt7, Grt14 and Grt15	2	NUTS	20.02	8,732	800
KADMOS	Muscovite	2	Direct Search	0.23	10,000	-
KADMOS	Muscovite	2	NUTS	0.55	999	100
KADMOS	Muscovite	3	Direct Search	44.28	1,000,000	-
KADMOS	Muscovite	3	NUTS	5.78	9,541	600
KADMOS + GDIFF	Grt7, Grt14, Grt15 and Muscovite	3	NUTS	25.1	13,780	400

To quantify the goodness of fit between modeled and observed data, we used a misfit function similar to Equation (4):

$$\begin{aligned} J_{\text{garnet}} = \sum_{i=1}^{k}\sum_{j=1}^{n} & w_{\text{Alm}} \left(\text{Alm}_{\text{model}}^{i,j} - \text{Alm}_{\text{obs}}^{i,j}\right)^2 + w_{\text{Grs}} \left(\text{Grs}_{\text{model}}^{i,j} - \text{Grs}_{\text{obs}}^{i,j}\right)^2 \\ & + w_{\text{Prp}} \left(\text{Prp}_{\text{model}}^{i,j} - \text{Prp}_{\text{obs}}^{i,j}\right)^2 + w_{\text{Sps}} \left(\text{Sps}_{\text{model}}^{i,j} - \text{Sps}_{\text{obs}}^{i,j}\right)^2 \end{aligned} \tag{11}$$

Here, Alm, Grs, Prp, and Sps indicate the almandine, grossular, pyrope, and spessartine components of garnet in mole fraction, respectively. n is the number of spatial points (i.e., measurements) and k is the total number of garnets (in this case, $k = 3$). With this misfit definition, the three different garnets (Grt7, Grt14, and Grt15) are considered together. The factor w corresponds to the associated weights attributed to each individual component. Weighting factors were considered to evaluate the influence of the grossular component on the misfit calculation. The importance of this lies in the fact that, among Mg, Fe, Mn, and Ca, Ca exhibits the slowest diffusion in garnet (Chakraborty & Ganguly, 1992). Also, the grossular component in the studied garnets shows the sharpest compositional gradients. A numerical spatial resolution of 100 grid points was adopted for all models. Finally, we used a numerical timestep of 0.02 Myr, which ensures that the modeled profiles have an error well below 1% associated with the temporal resolution (Figure S5).

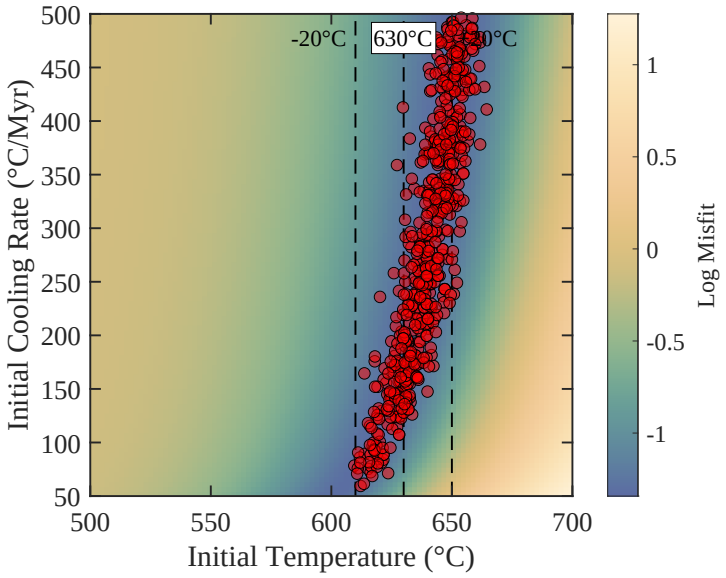

Figure 4: Combined misfit map generated using a direct search method integrating three different garnets (Grt7, Grt14 and Grt15). This map is presenting the goodness of fit between the modeled GDIFF output and the natural observations. Each combination of initial temperature and initial cooling rate represents a unique model evaluation and produces a unique misfit value. A low-misfit region (colored in blue) is identified. The combinations of parameters that fall inside this low-misfit zone are able to reproduce the compositional profiles of all three garnets. Interestingly, the low-misfit region coincides with independent thermobarometric estimations (630 ± 20 °C; Moutzouris et al., 2025). The red points represent the accepted HMC samples that were independently used to explore this parameter space. Notice that fewer samples are required to explore the parameter space with HMC (see main text).

The results of the direct search approach, assuming equal weights across all garnet endmembers, are presented in Figure 4. Figure 4 was created by summing the individual misfit maps for the three modeled garnets and displays the total misfit on a logarithmic scale. In this map, each combination of initial temperature and initial cooling rate corresponds to a unique misfit value. It is apparent that initial equilibration temperatures below $\sim$ 600 °C fail to reproduce the profiles of the three garnets for any cooling rate, as they produce large misfits. The same holds true for initial temperatures higher than $\sim$ 675 °C. However, a well-defined zone of low-misfit values is observed (blue area in Figure 4). This zone clusters around an initial temperature between 600 and 650 °C for any choice of cooling rate, which is remarkably close to the independent constraint of 630 ± 20 °C inferred in Moutzouris et al. (2025). We further explored the influence of assigning a higher weighting factor to the grossular component on the misfit calculation. Assuming that the contribution of grossular to the misfit is ten times greater than that of the other components,

the low-misfit zone remains virtually unchanged (Figure S6), corroborating the robustness of our approach.

We now discuss the exploration of the same parameter space between initial temperature and initial cooling rate using HMC. As with the direct search approach, we use the same asymptotic cooling path of Equation (10) until a final temperature of 300 °C. The prior probability distribution for the initial temperature was assumed to follow a Gaussian distribution, $\mathcal{N}(630, 20)$, following the independent thermobarometric results of Moutzouris et al. (2025), with a mean value of 630 °C and a standard deviation of 20 °C. Since there is no available constraint on the distribution of the initial cooling rate (e.g., Gaussian), we used a uniform prior ranging from 50 to 500 °C/Myr. The uniform distribution assumes that all values between 50 and 500 °C/Myr have equal initial probability of reproducing the data. For the likelihood specification in Turing.jl, the observed concentrations at each spatial point are modeled as normally (Gaussian) distributed around the corresponding model predictions. The errors between different spatial points are assumed to be independent. We considered a measurement uncertainty of 0.01 (i.e., 1 %) for each spatial point and across all compositional end-members of garnet. This is equivalent to assigning the same weighting factor for all endmembers. A total number of 600 posterior samples were generated for the combined parameter space of the three garnets to ensure convergence. We adopted the NUTS sampler which is defined by an initial "warm-up" (also known as "burn-in") phase during which the step size of the algorithm and the mass matrix are adapted. Finally, a random seed of 44 was used for all models to ensure reproducibility.

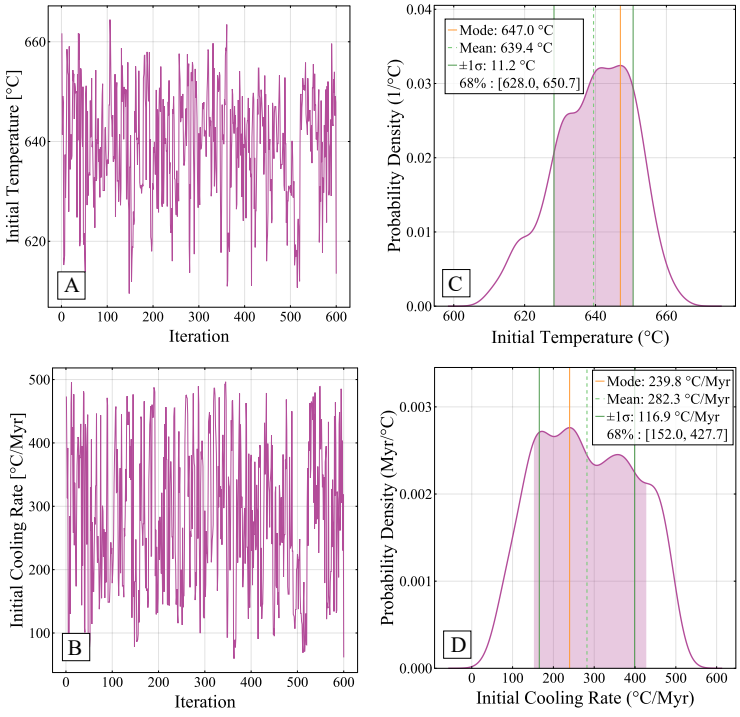

Figure 5: Trace plots (A, B) and posterior distributions (C, D) for initial temperature and initial cooling rate acquired using an HMC approach and GDIFF for the combined parameter space of the three investigated garnets. The trace plots display the parameter values accepted by the algorithm over successive iterations. The posterior distributions quantify the uncertainties on the invertible parameters. The inverted initial temperature distribution is Gaussian. The initial cooling rate shows a uniform distribution with various cooling rates being able to reproduce the observed data. The mean, standard deviation, mode and the typical sets are also presented in the legends of each posterior plot (see also main text). The initial cooling rate has a 68 % probability of lying between 152.0 and 427.7 °C/Myr.

The results of the HMC simulation for the combined parameter space of the three garnets are shown in Figure 5. Figures 5A and 5B present accepted sample values of initial temperature and cooling rate across iterations. These plots are also referred to as trace plots and they show the values of each variable that have been progressively accepted. Trace plots can be useful to determine the convergence of the algorithm. Convergence occurs when the trace plot shows no large-scale trend or drift. This indicates that the samples are exploring the posterior distribution efficiently. The trace plots presented in Figure 5 show no systematic trends which is indicative of convergence of the algorithm.

The accepted samples acquired with HMC can be used to infer statistics and quantify uncertainties on the invertible parameters. Figures 5C and 5D show the posterior probability distributions for initial temperature and cooling rate. The peaks of the posterior curves show the parameter values with the highest probability of reproducing the observed garnet compositions. These values represent the modes. The posterior distribution of initial temperature (Figure 5C) shows Gaussian characteristics. The mode of the initial temperature is at 647.0 °C. The mean and standard deviation of the initial temperature are 639.4 ± 11.2 °C. Figure 5C also indicates a 68 % probability that the initial temperature lies between 628.0 and 650.7 °C. The initial cooling rate shows a uniform behavior with negligible peaks of high probability (Figure 5D). This shows that a wide range of initial cooling rates reproduce the data similarly well. The mean and standard deviation of the initial cooling rate are 282.3 ± 116.9 °C/Myr. The mode is at 239.8 °C/Myr and 68 % of the probability mass lies between 152.0 and 427.7 °C/Myr.

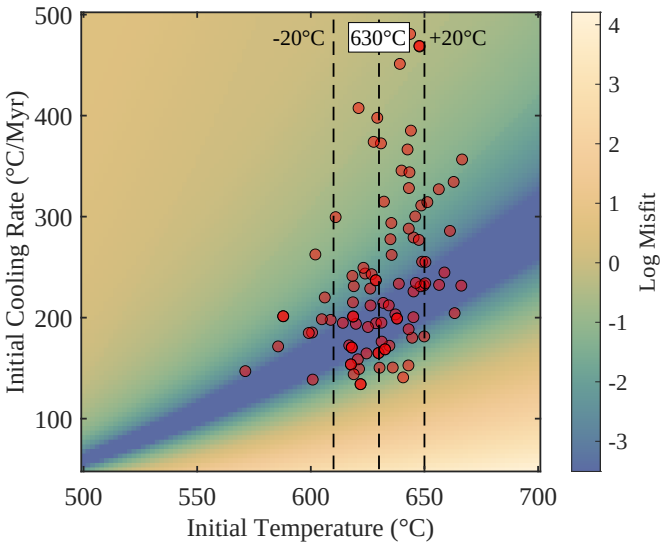

Figure 6: Calculated misfit map created based on a direct search approach for the $^{40}Ar/^{39}Ar$ age of muscovite. This map presents the goodness of fit between the modeled KADMOS output and the measured $^{40}Ar/^{39}Ar$ age of muscovite in our sample. A low-misfit region (blue colors) is identified. Assuming an initial temperature of approximately 630 °C, a cooling rate of approximately 200 °C/Myr is inferred. The red points represent the accepted HMC samples that were independently used to explore this parameter space based on KADMOS.

Direct comparison of the posterior samples and distributions with the misfit maps shows that HMC can identify and focus the sampling exclusively inside the low-misfit zone (Figure 4). Noticeably, for the case of two parameters, the total computation time was several times higher compared to the direct search approach (Table 1). We considered cases with fewer samples that resulted in lower total computational time but convergence was not possible as the posterior of the initial cooling rate showed bimodality.

4.3 KADMOS: Inversion with three parameters

KADMOS was used to fit the apparent $^{40}Ar/^{39}Ar$ age of muscovite (164.16 ± 0.37 Myr, Moutzouris et al., 2025) from the Pindos metamorphic sole. As with GDIFF, a direct search approach was initially used to invert only for initial temperature and cooling rate. We assumed a spherical geometry and a muscovite grain size of 20 μm. Diffusion data were taken from Harrison et al. (2009). Pressure was again fixed at 1.1 GPa. We used a resolution of 100 elements and an adaptive grid to capture sharp concentration gradients near the muscovite rim (see Appendix E for more details). The Ar concentration at the rim of muscovite was set to zero (i.e., Dirichlet boundary condition) to simulate argon escape. A zero-flux (i.e., Neumann) boundary condition was applied at the core of muscovite due to symmetry. We assumed an asymptotic cooling path (Equation 16) and varied the initial temperature between 500 and 700 °C. The initial cooling rate ranged from 50 to 500 °C/Myr. We used a parameter grid with a resolution of 100 for each variable.

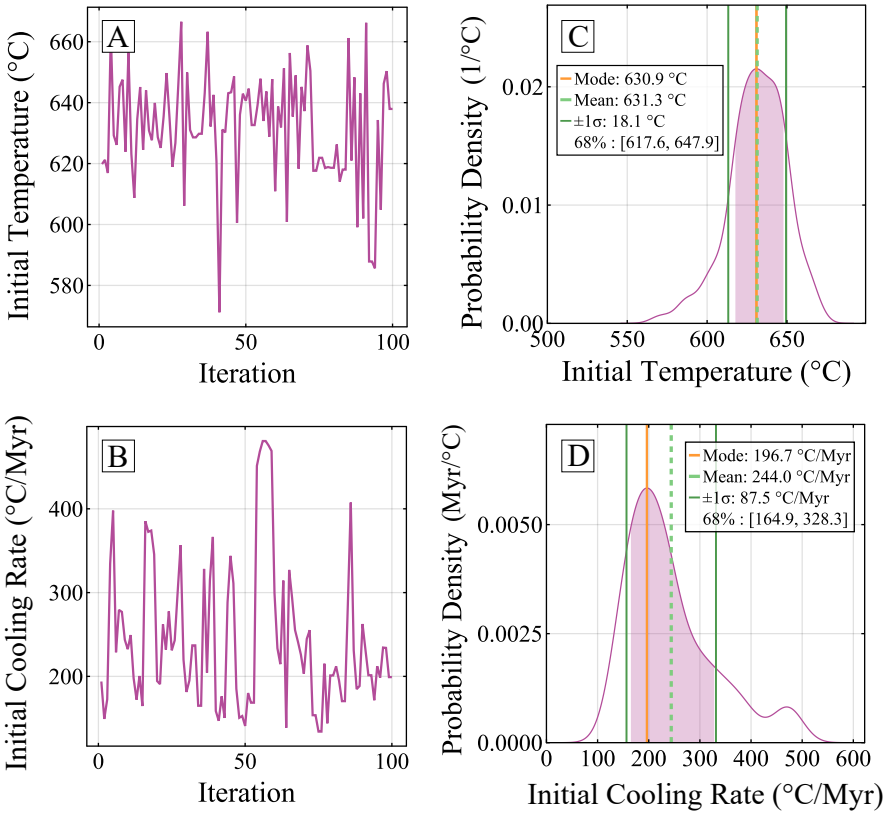

Figure 7: Trace plots (A, B) and posterior distributions (C, D) for initial temperature and initial cooling rate acquired using HMC and KADMOS in a two-dimensional parameter space. Both posterior distributions show a Gaussian behavior and efficiently sample the parameter space showing the values of initial cooling rate and temperature that are able to reproduce the muscovite age with significant probability. The initial cooling rate has a 68 % probability of lying between 164.9 and 328.3 °C/Myr with the most probable value being at 196.7 °C/Myr.

In this case, the misfit is simply calculated as:

$$J_{\text{muscovite}} = \left(t_{\text{model}}^{\text{muscovite}} - t_{\text{obs}}^{\text{muscovite}}\right)^2 \tag{12}$$

where $t_{\text{model}}^{\text{muscovite}}$ is the core (maximum) age of the modeled profile in each model evaluation and $t_{\text{obs}}^{\text{muscovite}}$ is equal to 164.16 Myr. Finally, a numerical timestep of 0.27 Myr was chosen, as it produces relative errors below 0.1% (Figure S7).

Based on the findings of Moutzouris et al. (2025), we assume that the metamorphic sole metapelite from the Pindos ophiolite was metamorphosed together with the associated amphibolites. This is favored due to the spatial and geochronological relationship between the two rocks. Therefore, we assume that the age of hornblende from the amphibolite corresponds to the age of peak metamorphic conditions. As a consequence, we used a total model duration of 165.5 Myr for the KADMOS models.

The results of direct search for two parameters with KADMOS are shown in Figure 6. A narrow field of low misfits is identified (blue region). In this case, the low-misfit zone indicates that the models are sensitive with respect to the initial cooling rate but not as much to the initial temperature. This is the opposite behavior compared to GDIFF. If we assume, based on petrological constraints, initial temperatures of 630, 650, and 610 °C, which correspond to previous thermobarometric results (630 ± 20 °C), then the implied cooling rates are approximately 185, 205, and 160 °C/Myr, respectively.

The HMC approach was implemented using the same asymptotic cooling (Equation 10). We used a uniform prior distribution for initial cooling rate ranging from 50 to 500 °C/Myr, following the same logic as in the models with GDIFF. A total of 100 posterior samples were drawn using NUTS. The measured uncertainty of the $^{40}Ar/^{39}Ar$ age of muscovite (± 0.37 Myr) was used for the evaluation of the likelihood.

The results of HMC using KADMOS for two parameters are presented in Figure 7, and more details on the HMC runs are found in Table 1. Based on the trace plots (Figures 7A and 7B), convergence has been achieved. Figures 7C and 7D show that the posterior distributions are well-behaved and Gaussian. The mode of initial temperature coincides well with the mean value at $\sim$ 630 °C. The 68% probability region lies between $\sim$ 617.6 and 647.9 °C. For the initial cooling rate, the mean value and standard deviation are 244.0 ± 87.5 °C/Myr. The mode lies at a value of 196.7 °C/Myr and the 68% probability region is within 164.9 and 328.3 °C/Myr. Interestingly, Figure 7D indicates that cooling rates above 300 °C/Myr also show a considerable probability of reproducing the observed age of muscovite within its uncertainty. This is not immediately evident by exclusively using the misfit map produced with direct search (Figure 6). It is also important to notice that the observed muscovite age cannot be reproduced by cooling rate values below $\sim$ 100 °C/Myr (Figures 7B, 7D and 6). Finally, in this case, HMC explored the parameter space in a computational time comparable to that of the direct search approach (Table 1).

In the previous two-dimensional example, the grain size was assumed to be equal to 20 μm. However, this parameter is unknown since multiple grain sizes are measured during the acquisition of the $^{40}Ar/^{39}Ar$ age. For this reason, we tested inverting additionally for an effective grain size. This makes the inversion problem three-dimensional, with initial temperature, initial cooling rate, and effective grain size as parameters. A direct search approach was initially used in which we evaluated models for all possible combinations between initial temperature, cooling rate, and effective grain size. The effective grain size ranged from 5 to 70 μm. We discretized the parameters with a resolution of 100, which resulted in 1,000,000 KADMOS model evaluations and a total computation time of 44.28 hours (Table 1). Misfits were plotted in a three-dimensional cube (Figure S8). Figure S8 shows a well-defined low-misfit zone. The vertical shape of this low-misfit zone shows that the fit of the muscovite age does not significantly depend on the effective grain size.

The three-dimensional parameter space was subsequently explored with HMC to check for the consistency of the inversion results. The prior distribution of the effective grain size was assumed uniform, ranging from 5 to 70 μm. The priors for initial temperature and cooling rate were kept the same as in the two-dimensional case. We drew a total of 600 samples to explore the three-dimensional parameter space. For this number of samples, a total of 9,541 KADMOS model evaluations were needed, and convergence was achieved in 5.8 hours of computation time (Table 1). The accepted samples in the three-dimensional parameter space are plotted as black points in Figure S8. The posterior distributions based on the accepted samples are plotted in Figure 8. All parameters show convergence based on their corresponding trace plots (Figures 8A to 8C). The initial temperature and cooling rate posterior distributions (Figures 8D and 8E) show identical behavior compared to the two-dimensional case (Figure 7). The 68% probability region for initial temperature lies between 612.5 and 651.2 °C while the mode is at 633.2 °C. The 68% probability region for the initial cooling rate is between 153.5 and 320.6 °C/Myr and the

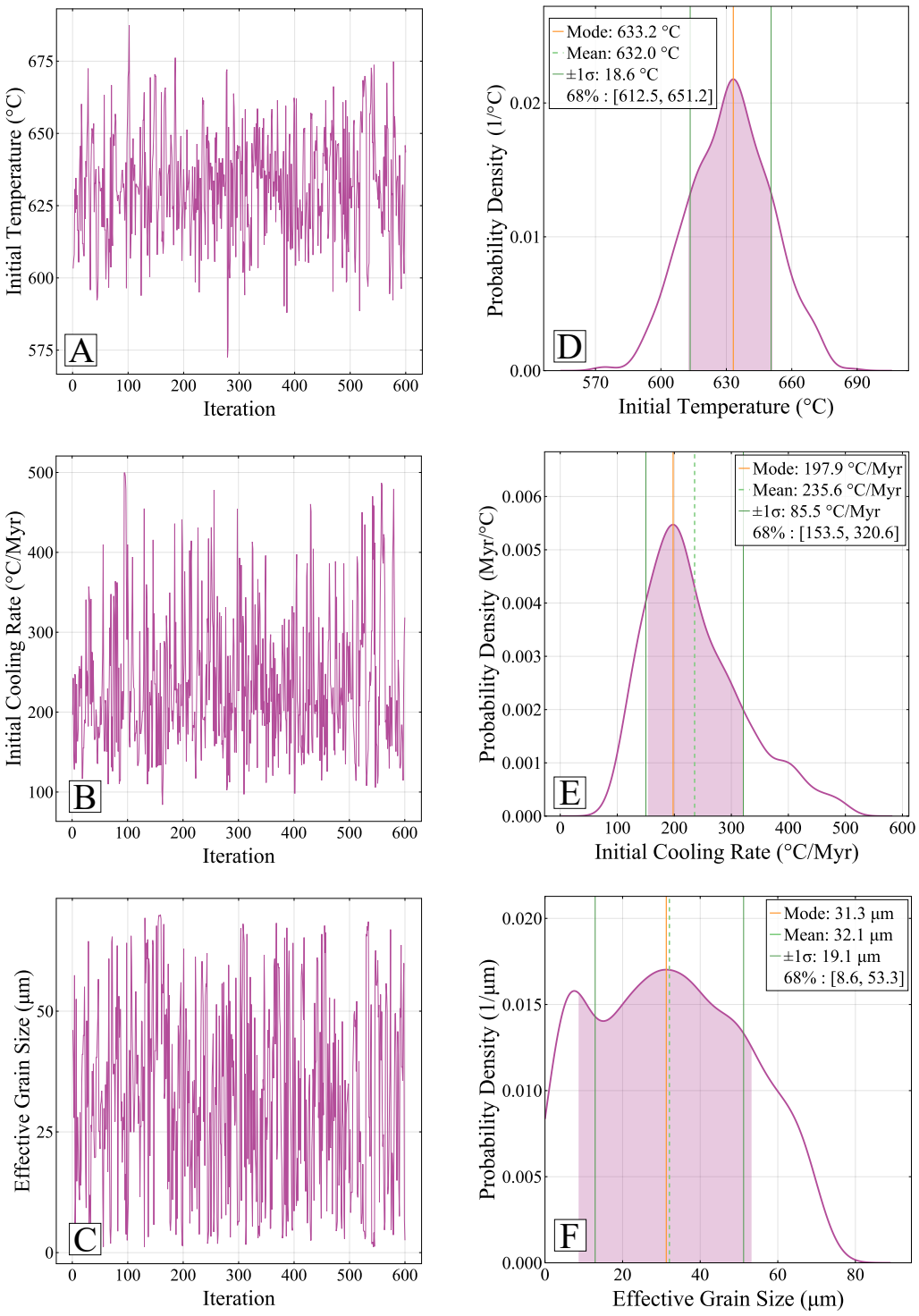

Figure 8: Trace plots (A, B, C) and posterior distributions (D, E, F)) for initial temperature, initial cooling rate and effective grain size acquired using HMC and KADMOS in the three-dimensional parameter space. The posterior distributions of initial temperature and cooling rate show the same Gaussian distribution as in the two-dimensional case (Figure 7). The effective grain size shows a uniform distribution, indicating that it does not affect the fit of the muscovite age significantly.

mode is at 197.9 °C/Myr. The effective grain size shows an almost uniform posterior distribution (Figure 8F), indicating that it is uninformative and does not contribute significantly to constraining the muscovite age. The minor degree of bimodality in the posterior distribution of the effective grain size may reflect the fact that a slightly larger sample size is required to fully resolve its structure.

4.4 Joint inversion

Sections 3.3 and 3.4 presented inversion results from two physically independent modeling systems. To identify the conditions that satisfy both systems simultaneously, the misfits from Figure 4 and Figure 6 can be combined. The two independent misfit maps were first normalized with their respective maximum values to ensure that they are dimensionless and comparable in magnitude. The normalized misfit maps were then added. The resulting combined map, shown in Figure 9, highlights the region where low-misfit zones from the two individual systems overlap. This optimal region can be identified between initial temperatures ranging from 610 to 650 °C and initial cooling rates from approximately 150 to 300 °C/Myr. The region represents the parameter combinations that simultaneously reproduce both garnet compositional profiles and the muscovite $^{40}Ar/^{39}Ar$ age. An absolute minimum misfit is found at an initial temperature of 631 °C and a cooling rate of 195 °C/Myr.

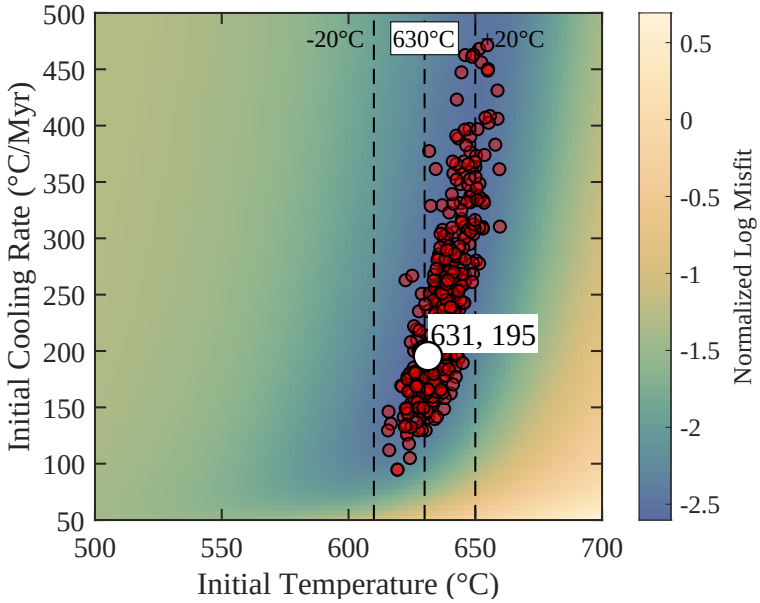

Figure 9: Combined misfit map showing the result after the addition of the individual misfit maps of Figures 4 and 6. This misfit map shows the combinations of initial temperature and cooling rate that are able to reproduce both garnet compositional profiles and the $^{40}Ar/^{39}Ar$ age of muscovite simultaneously. The low-misfit region (blue color) coincides well with previous thermobarometric (Moutzouris et al., 2025) results and shows a point with absolute minimum misfit at 631 °C and 195 °C/Myr. The red points correspond to the independently obtained HMC samples during this joint inversion.

Using HMC, we now systematically explore this combined parameter space and assess it statistically. This was done by combining GDIFF for the three different garnets and KADMOS for the muscovite and exploring the joint posterior distribution of the initial temperature, cooling rate, and effective grain size. In this way, HMC samples the joint likelihood surface directly, eliminating the need for separate inversions. For this analysis, we once more assumed a uniform prior on cooling rate ranging from 50 to 500 °C/Myr and a Gaussian prior on initial temperature, $\mathcal{N}(630, 20)$. The effective grain size was assumed to have a uniform prior ranging from 5 to 70 μm. A total of 400 samples were drawn, using the same uncertainty structure as in the previous sections. A random seed equal to 44 was once again used for reasons of reproducibility.

The results of the combined HMC approach are presented in Figure 10. Based on Figures 10A, 10B and 10C, the algorithm has converged. Figures 10D and 10E show that both the initial cooling rate and temperature are represented by well-behaved Gaussian posterior distributions. The initial temperature has a mean and standard deviation of 637.6 ± 8.3 °C. The mode is located at 638.1 °C and 68 % of the probability mass lies between 629.0 and 645.6 °C. The initial cooling rate has a mean and standard deviation of 241.3 ± 76.5 °C/Myr. The mode is found at 189.5 °C/Myr and 68 % of the probability mass is observed between 166.0 and 314.4 °C/Myr. The effective grain size, shown in Figure 10F, shows a uniform posterior distribution with the 68 % probability region lying between 10.0 and 55.3 µm. The HMC-derived samples map the low-misfit region that satisfies both physical models (Figure 9). Based on the accepted initial cooling rates and initial equilibration temperatures, the resulting cooling paths are illustrated in Figure S9. Finally, Figures 9 and 10 show that initial cooling rates in excess of 100 °C/Myr are needed to reproduce the investigated natural data from the Pindos metamorphic sole.

5 Discussion

5.1 Hamiltonian Monte Carlo: a powerful tool in petrology

The vast majority of geoscientific problems require some form of inversion to extract meaningful parameters capable of explaining either experimental or natural observations. In many cases, the inversion is inherently complex because a large set of parameters must be constrained simultaneously (e.g., Baumann & Kaus, 2015). Specifically in the field of petrology, inversion is commonly needed to extract key properties from experimental data such as diffusion rates of trace and major elements in different kinds of minerals (e.g., Chakraborty & Ganguly, 1992; Cherniak et al., 2007; Müller et al., 2013). In other cases, such as the one presented here, inversion quantifies parameters that help elucidate natural processes and reveal broader geodynamic implications. Additionally, the field of petrology is experiencing rapid advancements in numerical and analytical methods which are accompanied by an increasing abundance of useful data. These developments create opportunities to explore and test more complex hypotheses based on physical models. Therefore, inversion algorithms capable of operating in increasingly high-dimensional spaces are required.

In this paper, we demonstrate how HMC is a powerful tool to perform inversion for diffusion models involving two and three invertible parameters. In all of the two-parameter test cases, HMC required substantially fewer model evaluations than a direct search approach with comparable resolution (Table 1). Each accepted sample in HMC is defined by heavier computations due to the need of gradient information (here performed with Automatic Differentiation). This made the HMC exploration in the two-parameter cases slower than direct search. We also notice that in cases such as GDIFF, in which the posterior distribution can be uniform, HMC requires many more total samples to converge towards the final uniform state. HMC can also face difficulties when the posterior distribution is highly curved or strongly multimodal (Betancourt, 2018). However, the uniform character of a probability distribution can already be identified with a relatively small number of samples by the presence of an extended typical set (i.e., the 68 % probability region). In cases such as KADMOS, where the posterior is Gaussian, HMC converges significantly faster. HMC can also be significantly faster if multiple chains are computed with parallel threading. The implementation of this capability is however left for future work.

The reduction of total model evaluations becomes significant as model complexity increases. For higher-dimensional inversions, the scaling advantage of HMC becomes pronounced. This is because the computational cost of a direct search approach grows exponentially with the number of parameters while HMC maintains efficient exploration by using gradient information to reach the typical set rapidly. This behavior is reflected in our three-dimensional test cases. In these experiments, sufficient exploration of the typical set was achieved in just 5.8 hours instead of the 44 hours needed based on direct search (KADMOS). To explore the typical set for three parameters using both KADMOS and GDIFF only 25.1 hours were needed. Another advantage of HMC is that it avoids drifting in random directions because of the gradient information. This is a common problem in algorithms such as the Random Walk Metropolis (Betancourt, 2018).

The ability of HMC to efficiently handle high-dimensional parameter spaces allows posterior distributions to be readily evaluated and visualized. Even in the two-parameter cases where HMC

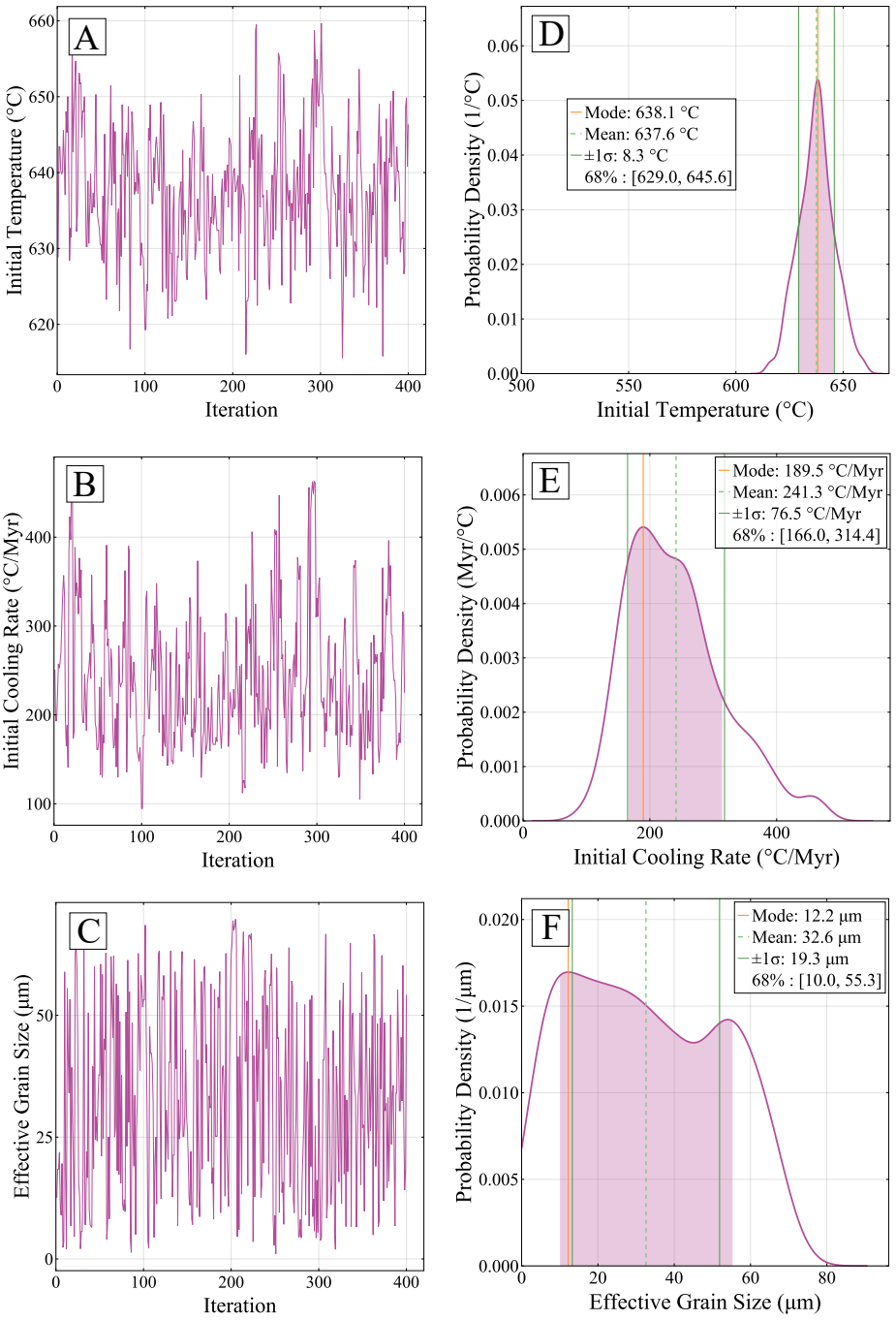

Figure 10: Trace plots (A, B) and posterior distributions (C, D) for initial cooling rate and temperature acquired using HMC for the joint parameter space of GDIFF and KADMOS. A cooling rate of 241.3 ± 76.5 °C/Myr is able to reproduce the entire petrological dataset for the Pindos metamorphic sole rocks.

may be slower, it still offers important benefits. It provides a rigorous statistical basis for quantifying uncertainties. Importantly, this approach also enables the assignment of uniform prior distributions to poorly constrained parameters and allows their influence on the data fit to be systematically evaluated. In our case, this is illustrated by the estimation of the effective grain size, which appears to have only a minor impact on the fit compared to the dominant control exerted by the initial cooling rate and equilibration temperature. Moreover, HMC algorithms such as the optimized NUTS are designed to eliminate the need for manual tuning. However, it must be stressed that the advantages of HMC heavily rely on the differentiability of the underlying numerical model. Despite these limitations, gradient-based inversion methods such as HMC drastically expand the range of problems that can be tackled in petrology. They enable the future integration of more complex thermomechanical or geodynamic models and open new opportunities to test scientific hypotheses. They finally allow the joint inversion and rigorous statistical quantification of different, independent physical systems in a simultaneous manner.

5.2 Geodynamic implications for the Pindos Metamorphic sole

Our investigation reveals the importance of combining petrological data with multiple independent modeling approaches. One of the key findings in the present work is the independent agreement between the GDIFF modeling results, the $^{40}Ar/^{39}Ar$ apparent age modeling of muscovite, and previously published thermobarometric and geochronological data for the Pindos metamorphic sole (Moutzouris et al., 2025). In particular, Figure 4 shows that the observed garnet compositional profiles can only be reproduced if the investigated garnet-schist started cooling from $\sim$ 630 °C. This temperature is in excellent agreement with the thermobarometric estimates of Moutzouris et al. (2025). Moreover, our joint inversion approach strongly suggests that an initial cooling rate of 241.3 $\pm$ 76.5 °C/Myr is able to simultaneously explain thermobarometry, the major-element zoning in garnet, and the measured $^{40}Ar/^{39}Ar$ muscovite age. This result is consistent with cooling rates previously inferred from geochronological data for the Pindos metamorphic sole (Moutzouris et al., 2025). Similar agreement between garnet diffusion modeling and geochronological constraints has been documented for the Main Central Thrust in the Sikkim Himalaya (Burg & Moulas, 2022). Here, we demonstrate that integrating multiple, independently derived datasets reinforces the robustness of the inferred evolution of an investigated rock.

The calculated cooling rate of 241.3 $\pm$ 76.5 °C/Myr was acquired using an asymptotic temperature–time path. This kind of cooling path is considered reasonable for several reasons. The preservation of the sharp gradients in the slow diffusing grossular component in combination with the preservation of the fast diffusing Mg, Fe, and Mn profiles is a strong indication of a short residence time at high-temperature conditions (e.g., Ague & Baxter, 2007). An opposite scenario, in which the rocks cool progressively faster towards the surface, would translate into a long residence time at high-temperature conditions. This prolonged residence time would eliminate the sharp gradients of Ca and the diffusion profiles of Mg, Fe, and Mn. In addition, such a scenario would lead to the relaxation of the residual pressure of quartz inclusions in garnet (Zhong et al., 2018, 2020). The chosen asymptotic path additionally agrees well with previous data from the Oman ophiolite (Hacker et al., 1996). It is further compatible with previous numerical work on metamorphic soles (Duretz et al., 2016; Ibragimov et al., 2024). These arguments, along with the results presented in this work, strongly support that the attainment of peak conditions was followed by asymptotic rapid cooling with an initial cooling rate of 241.3 $\pm$ 76.5 °C/Myr.

The excessive values of inferred cooling rates, even though they are transient in character, require a physical mechanism in order to be explained. Based on our findings, two different scenarios can be considered. According to the first scenario, the metamorphic sole could be formed due to deep-burial metamorphism at depths exceeding 30 km (Agard et al., 2016; Ambrose et al., 2021; Guilmette et al., 2018; Mulder et al., 2016; Searle & Cox, 1999; Searle et al., 2015). In this scenario, the inverted metamorphic gradients found in metamorphic soles along with the high temperatures of equilibration are explained by the existence of a hot overlying mantle wedge and due to conductive heat transport (Jamieson, 1986). The exhumation of the ophiolite, and therefore the metamorphic sole, in such a setting is usually thought to occur along the subduction interface and driven by buoyancy (e.g., Cowan et al., 2014).

The second scenario postulates the significance of rapid metamorphism during incipient intra-

oceanic thrusting (Duretz et al., 2016; Ibragimov et al., 2024). In this scenario, numerical modeling shows that the temperatures recorded by metamorphic soles can only be reached with the contribution of transient processes such as shear (frictional) heating, and that the high-temperature conditions are a function of the shearing velocity and the thermomechanical properties of the materials involved. Additionally, in a scenario of shear heating, it has been found that the cessation of shearing is followed by rapid asymptotic cooling as shown by Burg & Moulas (2022). The metamorphic pressures of equilibration could be explained due to the localization of tectonic stresses (Brown, 2023; Moulas et al., 2013; Zuza et al., 2022). More evidence for this theory has lately been suggested for the Samail ophiolite (Garber et al., 2025; Ibragimov et al., 2024).

Finally, in addition to the aforementioned studies, new results by Tagliaferri et al. (2025), based on garnet diffusion modelling and thermokinematic models, suggested that rocks directly adjacent to a shear zone cool at approximately 200 °C/Myr once deformation ceases. This estimation is directly comparable with our results since the aforementioned authors emphasized the importance of rapid shearing and potential shear heating in producing initial cooling rates in high-grade metamorphic rocks. In light of these results, and given the consistency between our findings and previous studies, we support that the metamorphic sole of the Pindos ophiolite was strongly influenced by shear heating and formed during the initiation of intra-oceanic subduction.

6 Conclusions

In this work, we demonstrate that joint inversion of multiple, independent systems is essential for furthering our understanding of metamorphic processes. Our study used the Pindos metamorphic sole as an example for inversion. Garnet diffusion indicated an initial equilibration temperature of about 630 °C. This result agrees, in an independent manner, with previous thermobarometric estimates. An advantage of our approach is that when garnet diffusion is combined with diffusion modeling of Ar in muscovite, the calculation of the cooling rates and the associated uncertainties is feasible and computationally efficient. In particular, we found that a cooling rate of 241.3 ± 76.5 °C/Myr is able to reproduce the recently published data from Pindos ophiolite (Moutzouris et al. 2025). To conclude, we find that the most likely explanation for the high cooling rates at high temperatures is the cessation of shearing and the associated thermal relaxation. In the present study, we highlight the value of Hamiltonian Monte Carlo as an inversion method. We showed that Hamiltonian Monte Carlo is a powerful tool to explore the investigated parameter space and provide a rigorous statistical analysis and uncertainty assessment. We suggest Hamiltonian Monte Carlo as an additional tool for future petrological studies where many parameters need to be explored, which requires efficient algorithms where simpler direct search methods are computationally too expensive.

Acknowledgments

E. Moulas and D. Moutzouris would like to acknowledge the German Research Foundation for financial support (DFG; project number 512790090). S. Schorn acknowledges the Alexander von Humboldt Foundation for support.

References

Agard, P., Yamato, P., Soret, M., Prigent, C., Guillot, S., Plunder, A., Dubacq, B., Chauvet, A., & Monié, P. (2016). Plate interface rheological switches during subduction infancy: Control on slab penetration and metamorphic sole formation. *Earth and Planetary Science Letters*, 451, 208–220. https://doi.org/10.1016/j.epsl.2016.06.054

Ague, J. J., & Baxter, E. F. (2007). Brief thermal pulses during mountain building recorded by Sr diffusion in apatite and multicomponent diffusion in garnet. *Earth and Planetary Science Letters*, 261(3–4), 500–516. https://doi.org/10.1016/j.epsl.2007.07.017

Ambrose, T. K., Waters, D. J., Searle, M. P., Gopon, P., & Forshaw, J. B. (2021). Burial, Accretion, and Exhumation of the Metamorphic Sole of the Oman-UAE Ophiolite. *Tectonics*, 40(4), e2020TC006392. https://doi.org/10.1029/2020TC006392

Arnold, V. I. (1974). Mathematical Methods of Classical Mechanics (Second, Vol. 60). Springer.

Bailer-Jones, C. A. L. (2017). Practical Bayesian Inference: A Primer for Physical Scientists. In Practical Bayesian Inference (1st ed.). Cambridge University Press. https://doi.org/10.1017/9781108123891.001

Batanova, V. G., Sobolev, A. V., & Magnin, V. (2018). Trace element analysis by EPMA in geosciences: Detection limit, precision and accuracy. *IOP Conference Series: Materials Science and Engineering*, 304, 012001. https://doi.org/10.1088/1757-899x/304/1/012001

Baumann, T. S., & Kaus, B. J. P. (2015). Geodynamic inversion to constrain the non-linear rheology of the lithosphere. *Geophysical Journal International*, 202(2), 1289–1316. https://doi.org/10.1093/gji/ggv201

Betancourt, M. (2018). A Conceptual Introduction to Hamiltonian Monte Carlo (1701.02434). *arXiv*. https://doi.org/10.48550/arXiv.1701.02434

Bezanson, J., Edelman, A., Karpinski, S., & Shah, V. B. (2017). Julia: A Fresh Approach to Numerical Computing. *SIAM Review*, 59(1), 65–98. https://doi.org/10.1137/141000671

Brown, M. (2023). Some thoughts about eclogites and related rocks. *European Journal of Mineralogy*, 35(4), 523–547. https://doi.org/10.5194/ejm-35-523-2023

Burg, J.-P., & Moulas, E. (2022). Cooling-rate constraints from metapelites across two inverted metamorphic sequences of the Alpine-Himalayan belt; evidence for viscous heating. *Journal of Structural Geology*, 156, 104536. https://doi.org/10.1016/j.jsg.2022.104536

Carpenter, B., Gelman, A., Hoffman, M. D., Lee, D., Goodrich, B., Betancourt, M., Brubaker, M., Guo, J., Li, P., & Riddell, A. (2017). Stan: A Probabilistic Programming Language. *Journal of Statistical Software*, 76(1). https://doi.org/10.18637/jss.v076.i01

Chakraborty, S., & Ganguly, J. (1992). Cation diffusion in aluminosilicate garnets: Experimental determination in spessartine-almandine diffusion couples, evaluation of effective binary diffusion coefficients, and applications. *Contributions to Mineralogy and Petrology*, 111(1), 74–86. https://doi.org/10.1007/BF00296579

Cheng, H., Bloch, E. M., Moulas, E., & Vervoort, J. D. (2020). Reconciliation of discrepant U–Pb, Lu–Hf, Sm–Nd, Ar–Ar and U–Th/He dates in an amphibolite from the Cathaysia Block in Southern China. *Contributions to Mineralogy and Petrology*, 175(1), 4. https://doi.org/10.1007/s00410-019-1644-9

Cherniak, D. J., Watson, E. B., & Wark, D. A. (2007). Ti diffusion in quartz. *Chemical Geology*, 236(1–2), 65–74. https://doi.org/10.1016/j.chemgeo.2006.09.001

Costa, F., Shea, T., & Ubide, T. (2020). Diffusion chronometry and the timescales of magmatic processes. *Nature Reviews Earth & Environment*, 1(4), 201–214. https://doi.org/10.1038/s43017-020-0038-x

Cowan, R. J., Searle, M. P., & Waters, D. J. (2014). Structure of the metamorphic sole to the Oman Ophiolite, Sumeini Window and Wadi Tayyin: Implications for ophiolite obduction processes. *Geological Society, London, Special Publications*, 392(1), 155–175. https://doi.org/10.1144/SP392.8

De Lima, P. D. S., Ferreira, M. S., Corso, G., & De Araújo, J. M. (2024). Bayesian time-lapse full waveform inversion using Hamiltonian Monte Carlo. *Geophysical Prospecting*, 72(9), 3381–3398. https://doi.org/10.1111/1365-2478.13604

Duane, S., Kennedy, A. D., Pendleton, B. J., & Roweth, D. (1987). Hybrid Monte Carlo. *Physics Letters B*, 195(2), 216–222. https://doi.org/10.1016/0370-2693(87)91197-X

Duretz, T., Agard, P., Yamato, P., Ducassou, C., Burov, E. B., & Gerya, T. V. (2016). Thermo-mechanical modeling of the obduction process based on the Oman Ophiolite case. *Gondwana Research*, 32, 1–10. https://doi.org/10.1016/j.gr.2015.02.002

Eidsvik, J., & Tjelmeland, H. (2006). On directional Metropolis–Hastings algorithms. *Statistics and Computing*, 16(1), 93–106. https://doi.org/10.1007/s11222-006-5536-2

Faryad, S. W., & Chakraborty, S. (2005). Duration of Eo-Alpine metamorphic events obtained from multicomponent diffusion modeling of garnet: A case study from the Eastern Alps. *Contributions to Mineralogy and Petrology*, 150(3), 306–318. https://doi.org/10.1007/s00410-005-0020-0

Fichtner, A., & Zunino, A. (2019). Hamiltonian Nullspace Shuttles. *Geophysical Research Letters*, 46(2), 644–651. https://doi.org/10.1029/2018gl080931

Fichtner, A., Zunino, A., Gebraad, L., & Boehm, C. (2021). Autotuning Hamiltonian Monte Carlo for efficient generalized nullspace exploration. *Geophysical Journal International*, 227(2), 941–968. https://doi.org/10.1093/gji/ggab270

Fjelde, T. E., Xu, K., Widmann, D., Tarek, M., Pfiffer, C., Trapp, M., Axen, S. D., Sun, X., Hauru, M., Yong, P., Tebbutt, W., Ghahramani, Z., & Ge, H. (2025). Turing.jl: A general-purpose probabilistic programming language. *ACM Transactions on Probabilistic Machine Learning*. https://doi.org/10.1145/3711897

Garber, J. M., Rioux, M., Smye, A. J., Cruz-Uribe, A. M., Baker, P. L., Vervoort, J. D., Searle, M. P., & Feineman, M. D. (2025). Shear heating during rapid subduction initiation beneath the Samail Ophiolite. *Nature Geoscience*, 18, 653–660. https://doi.org/10.1038/s41561-025-01711-6

Ge, H., Xu, K., & Ghahramani, Z. (2018). Turing: A language for flexible probabilistic inference.*Proceedings of the 21st International Conference on Artifcial Intelligence and Statistics*, 84.

Gebraad, L., Boehm, C., & Fichtner, A. (2020). Bayesian Elastic Full-Waveform Inversion Using Hamiltonian Monte Carlo. *Journal of Geophysical Research: Solid Earth*, 125(3), e2019JB018428. https://doi.org/10.1029/2019JB018428

Girolami, M., & Calderhead, B. (2011). Riemann Manifold Langevin and Hamiltonian Monte Carlo Methods. *Journal of the Royal Statistical Society Series B: Statistical Methodology*, 73(2), 123–214. https://doi.org/10.1111/j.1467-9868.2010.00765.x

Guilmette, C., Smit, M. A., Van Hinsbergen, D. J. J., Gürer, D., Corfu, F., Charette, B., Maffione, M., Rabeau, O., & Savard, D. (2018). Forced subduction initiation recorded in the sole and crust of the Semail Ophiolite of Oman. *Nature Geoscience*, 11(9), 688–695. https://doi.org/10.1038/s41561-018-0209-2

Hacker, B. R., Mosenfelder, J. L., & Gnos, E. (1996). Rapid emplacement of the Oman ophiolite: Thermal and geochronologic constraints. *Tectonics*, 15(6), 1230–1247. https://doi.org/10.1029/96TC01973

Hajian, A (2007). Efficient cosmological parameter estimation with Hamiltonian Monte Carlo technique. *Physical Review D*, 75(8). https://doi.org/10.1103/physrevd.75.083525

Harrison, T. M., Célérier, J., Aikman, A. B., Hermann, J., & Heizler, M. T. (2009). Diffusion of 40Ar in muscovite. *Geochimica et Cosmochimica Acta*, 73(4), 1039–1051. https://doi.org/10.1016/j.gca.2008.09.038

Hoffman, M. D., & Gelman, A. (2014). The No-U-Turn Sampler: Adaptively Setting Path Lengths in Hamiltonian Monte Carlo. *Journal of Machine Learning Research*, 15, 1593-1623.

Hastings, W. K. (1970). Monte Carlo sampling methods using Markov chains and their applications. *Biometrika*, 57(1), 97–109. https://doi.org/10.1093/biomet/57.1.97

Ibragimov, I., Kiss, D., & Moulas, E. (2024). A thermo-mechanical model of the thermal evolution and incorporation of metamorphic soles in Tethyan ophiolites: A case study from Oman. *Austrian Journal of Earth Sciences*, 117(1), 13–24. https://doi.org/10.17738/ajes.2024.0002

Jamieson, R. A. (1986). P-T paths from high temperature shear zones beneath ophiolites. *Journal of Metamorphic Geology*, 4(1), 3–22. https://doi.org/10.1111/j.1525-1314.1986.tb00335.x

Kabanikhin, S. I. (2008). Definitions and examples of inverse and ill-posed problems. *Journal of Inverse and Ill-Posed Problems*, 16(4). https://doi.org/10.1515/jiip.2008.019

Kelley, S. (2002). K-Ar and Ar-Ar Dating. *Reviews in Mineralogy and Geochemistry*, 47(1), 785–818. https://doi.org/10.2138/rmg.2002.47.17

Kent, A. J. R., Hutcheon, I. D., Ryerson, F. J., & Phinney, D. L. (2001). The temperature of formation of carbonate in martian meteorite ALH84001: Constraints from cation diffusion. *Geochimica et Cosmochimica Acta*, 65(2), 311–321. https://doi.org/10.1016/s0016-7037(00)00528-7

Koch, M. C., Fujisawa, K., & Murakami, A. (2020). Adjoint Hamiltonian Monte Carlo algorithm for the estimation of elastic modulus through the inversion of elastic wave propagation data. *International Journal for Numerical Methods in Engineering*, 121(6), 1037–1067. https://doi.org/10.1002/nme.6256

Kohn, M. J., & Spear, F. (2000). Retrograde net transfer reaction insurance for pressure-temperature estimates. *Geology*, 28(12), 1127. https://doi.org/10.1130/0091-7613(2000)28%253C1127:rntrif%253E2.0.co;2

Lasaga, A. C. (1979). Multicomponent exchange and diffusion in silicates. *Geochimica et Cosmochimica Acta*, 43(4), 455–469. https://doi.org/10.1016/0016-7037(79)90158-3

Lasaga, A. C. (1983). Geospeedometry: An Extension of Geothermometry. In S. K. Saxena (Ed.), *Kinetics and Equilibrium in Mineral Reactions (Vol. 3, pp. 81–114)*. Springer New York. https://doi.org/10.1007/978-1-4612-5587-1_3

Lasaga, A. C., Richardson, S. M., & Holland, H. D. (1977). The Mathematics of Cation Diffusion and Exchange Between Silicate Minerals During Retrograde Metamorphism. In S. K. Saxena, S. Bhattacharji, H. Annersten, & O. Stephansson (Eds.), *Energetics of Geological Processes* (pp. 353–388). Springer Berlin Heidelberg. https://doi.org/10.1007/978-3-642-86574-9_15

Liati, A., Gebauer, D., & Fanning, C. M. (2004). The age of ophiolitic rocks of the Hellenides (Vourinos, Pindos, Crete): First U–Pb ion microprobe (SHRIMP) zircon ages. *Chemical Geology*, 207(3–4), 171–188. https://doi.org/10.1016/j.chemgeo.2004.02.010

Mackay-Champion, T., & Cawood, I. P. (2025). An Inverse Method for Quantifying Petrological Parameters and Uncertainty in Phase Equilibrium Modelling. *Journal of Metamorphic Geology*, jmg.70016. https://doi.org/10.1111/jmg.70016

Medaris, L. G., Wang, H. F., Mísař, Z., & Jelínek, E. (1990). Thermobarometry, diffusion modelling and cooling rates of crustal garnet peridotites: Two examples from the Moldanubian zone of the Bohemian Massif. *Lithos*, 25(1–3), 189–202. https://doi.org/10.1016/0024-4937(90)90014-r

Mehlig, B., Heermann, D. W., & Forrest, B. M. (1992). Hybrid Monte Carlo method for condensed-matter systems. *Physical Review B*, 45(2), 679–685. https://doi.org/10.1103/physrevb.45.679

Metropolis, N., Rosenbluth, A. W., Rosenbluth, M. N., Teller, A. H., & Teller, E. (1953). *Equation of State Calculations by Fast Computing Machines.* The Journal of Chemical Physics, 21(6), 1087–1092. https://doi.org/10.1063/1.1699114

Mikkola, S., & Tanikawa, K. (1999). Explicit Symplectic Algorithms for time-transformed Hamiltonians. *Celestial Mechanics and Dynamical Astronomy*, 74, 287–295.

Moulas, E. (2023). GDIFF: A Finite Difference code for the calculation of multicomponent diffusion in garnet (Version v 1.2) [Computer software]. *Zenodo.* https://doi.org/10.5281/ZENODO.7805989

Moulas, E., & Brandon, M. T. (2022). KADMOS: A Finite Element code for the calculation of apparent K-Ar ages in minerals (Version 1) [Computer software]. *Zenodo.* https://doi.org/10.5281/ZENODO.7358138

Moulas, E., Podladchikov, Y. Y., Aranovich, L. Ya., & Kostopoulos, D. (2013). The problem of depth in geology: When pressure does not translate into depth. *Petrology*, 21(6), 527–538. https://doi.org/10.1134/S0869591113060052

Moutzouris, D., Moulas, E., Kostopoulos, D., Pomonis, P., Beranoaguirre, A., Chatzitheodoridis, E., & Gerdes, A. (2025). Emplacement of the Pindos ophiolite, NW Greece: P-T-t-kinematic constraints from the metamorphic sole. *Lithos*, 516–517(108285). https://doi.org/10.1016/j.lithos.2025.108285

Mulder, J. A., Berry, R. F., Meffre, S., & Halpin, J. A. (2016). The metamorphic sole of the western Tasmanian ophiolite: New insights into the Cambrian tectonic setting of the Gondwana Pacific margin. *Gondwana Research*, 38, 351–369. https://doi.org/10.1016/j.gr.2015.12.010

Müller, T., Dohmen, R., Becker, H. W., Ter Heege, J. H., & Chakraborty, S. (2013). Fe–Mg interdiffusion rates in clinopyroxene: Experimental data and implications for Fe–Mg exchange geothermometers. *Contributions to Mineralogy and Petrology*, 166(6), 1563–1576. https://doi.org/10.1007/s00410-013-0941-y

Neal, R. M. (1996). Bayesian Learning for Neural Networks. Springer New York. https://doi.org/10.1007/978-1-4612-0745-0

Neal, R. M. (2011). MCMC using Hamiltonian dynamics. https://doi.org/10.1201/b10905

Neidinger, R. D. (2010). Introduction to Automatic Differentiation and MATLAB Object-Oriented Programming. *SIAM Review*, 52(3), 545–563. https://doi.org/10.1137/080743627

Olker, B., Altherr, R., & Paquin, J. (2003). Fast exhumation of the ultrahigh-pressure Alpe Arami garnet peridotite (Central Alps, Switzerland): Constraints from geospeedometry and thermal modelling. *Journal of Metamorphic Geology*, 21(4), 395–402. https://doi.org/10.1046/j.1525-1314.2003.00450.x

Reuber, G. S. (2021). Statistical and deterministic inverse methods in the geosciences: Introduction, review, and application to the nonlinear diffusion equation. *GEM - International Journal on Geomathematics*, 12(1). https://doi.org/10.1007/s13137-021-00186-y

Revels, J., Lubin, M., & Papamarkou, T. (2016). Forward-Mode Automatic Differentiation in Julia *(No. arXiv:1607.07892). arXiv.* https://doi.org/10.48550/arXiv.1607.07892

Schorn, S., Moulas, E., & Stüwe, K. (2024). Exothermic reactions and 39Ar–40Ar thermochronology: Hydration leads to younger apparent ages. *Geology*, 52(6), 458–462. https://doi.org/10.1130/G51776.1

Schwarzenbach, E. M., Vogel, M., Früh-Green, G. L., & Boschi, C. (2021). Serpentinization, Carbonation, and Metasomatism of Ultramafic Sequences in the Northern Apennine Ophiolite (NW Italy). *Journal of Geophysical Research: Solid Earth*, 126(5), e2020JB020619. https://doi.org/10.1029/2020JB020619

Searle, M., & Cox, J. (1999). Tectonic setting, origin, and obduction of the Oman ophiolite. *Geological Society of America Bulletin*, 111(1). https://doi.org/10.1130/0016-7606(1999)111%253C0104:TSOAOO%253E2.3.CO;2

Searle, M. P., Waters, D. J., Garber, J. M., Rioux, M., Cherry, A. G., & Ambrose, T. K. (2015). Structure and metamorphism beneath the obducting Oman ophiolite: Evidence from the Bani Hamid granulites, northern Oman mountains. *Geosphere*, 11(6), 1812–1836. https://doi.org/10.1130/GES01199.1

Sen, M. K., & Biswas, R. (2017). Transdimensional seismic inversion using the reversible jump Hamiltonian Monte Carlo algorithm. *GEOPHYSICS*, 82(3), R119–R134. https://doi.org/10.1190/geo2016-0010.1

Spear, F. S. (2004). Fast Cooling and Exhumation of the Valhalla Metamorphic Core Complex, Southeastern British Columbia. *International Geology Review*, 46(3), 193–209. https://doi.org/10.2747/0020-6814.46.3.193

Tagliaferri, A., Moulas, E., Schmalholz, S. M., & Schenker, F. L. (2025). Fast and Spatially Heterogeneous Cooling Rates at Amphibolite-Facies Conditions in the Lepontine Alps (Switzerland). *Geochemistry, Geophysics, Geosystems*, 26(11), e2025GC012410. https://doi.org/10.1029/2025GC012410

Turner, G., Miller, J. A., & Grasty, R. L. (1966). The thermal history of the Bruderheim meteorite. *Earth and Planetary Science Letters*, 1(4), 155–157. https://doi.org/10.1016/0012-821X(66)90061-6

Xu, K., Ge, H., Tebbutt, W., Tarek, M., Trapp, M., & Ghahramani, Z. (2020). AdvancedHMC.jl: A robust, modular and efficient implementation of advanced HMC algorithms. *2nd Symposium on Advances in Approximate Bayesian Inference*, 118, 1–10.

Xu, Y., Chu, W., Huang, S., Guo, R., Lu, S., & Nan, F. (2025). Three-dimensional gravity inversion based on the Hamiltonian Monte Carlo method. *Geophysical Prospecting*, 73, 1301–1314. https://doi.org/10.1111/1365-2478.70016

Yoshida, H. (1990). Construction of higher order symplectic integrators. *Physics Letters A*, 150(5–7), 262–268. https://doi.org/10.1016/0375-9601(90)90092-3

Zhong, X., Moulas, E., & Tajčmanová, L. (2018). Tiny timekeepers witnessing high-rate exhumation processes. *Scientific Reports*, 8(1), 2234. https://doi.org/10.1038/s41598-018-20291-7

Zhong, X., Moulas, E., & Tajčmanová, L. (2020). Post-entrapment modification of residual inclusion pressure and its implications for Raman elastic thermobarometry. *Solid Earth*, 11(1), 223–240. https://doi.org/10.5194/se-11-223-2020

Zunino, A., Ghirotto, A., Armadillo, E., & Fichtner, A. (2022). Hamiltonian Monte Carlo Probabilistic Joint Inversion of 2D (2.75D) Gravity and Magnetic Data. *Geophysical Research Letters*, 49(20), e2022GL099789. https://doi.org/10.1029/2022GL099789

Zuza, A. V., Levy, D. A., & Mulligan, S. R. (2022). Geologic field evidence for non-lithostatic overpressure recorded in the North American Cordillera hinterland, northeast Nevada. *Geoscience Frontiers*, 13(2), 101099. https://doi.org/10.1016/j.gsf.2020.10.006

Appendices

A Conservation of Hamiltonian energy

In time-evolving physical systems, the Hamiltonian energy can be a function of time (t), position ($\boldsymbol{\theta}(t)$), and momentum ($\boldsymbol{p}(t)$). To keep the analogy between physical systems and inverse modelling, we note that the position vector corresponds to the vector of inverted parameters (θ_i) and the momentum vector corresponds to the vector of artificial momenta (p_i). For cases where the Hamiltonian energy $H(t, \boldsymbol{\theta}(t), \boldsymbol{p}(t))$ does not explicitly depend on time we have:

$$\frac{\partial H}{\partial t} = 0 \tag{A1}$$

Equation (A1) has important consequences for the conservation of the total energy in mechanical systems. Following Arnold (1974, p. 67), we can write the general equation for the time derivative of the Hamiltonian $H(t, \boldsymbol{\theta}(t), \boldsymbol{p}(t))$ as follows:

$$\frac{dH}{dt} = \frac{\partial H}{\partial t} + \sum_{j=1}^{k} \left[\frac{\partial H}{\partial \theta_i} \frac{d\theta_i}{dt} + \frac{\partial H}{\partial p_i} \frac{dp_i}{dt} \right] \tag{A2}$$

For the cases where Eq. (A1) holds, and by substituting the canonical equations (Equations 2 and 3 in the main text), Equation (A2) becomes:

$$\frac{dH(\boldsymbol{\theta}, \boldsymbol{p})}{dt} = \sum_{j=1}^{k} \left[-\frac{\partial H(\boldsymbol{\theta}, \boldsymbol{p})}{\partial \theta_i} \frac{\partial H(\boldsymbol{\theta}, \boldsymbol{p})}{\partial p_i} + \frac{\partial H(\boldsymbol{\theta}, \boldsymbol{p})}{\partial p_i} \frac{\partial H(\boldsymbol{\theta}, \boldsymbol{p})}{\partial \theta_i} \right] = 0 \tag{A3}$$

where we have emphasized that $H(\boldsymbol{\theta}, \boldsymbol{p})$ is not an explicit function of time even though $\boldsymbol{\theta}(t)$ and $\boldsymbol{p}(t)$ change in time. The last result shows that $H(\boldsymbol{\theta}, \boldsymbol{p})$ does not change in time and therefore, the Hamiltonian is conserved.

B HMC with the Bayesian approach

This section provides clarifications on the concepts behind the Bayesian approach of HMC that may be useful for the reader to understand the analogies between the two different available approaches (misfit and Bayesian formulation). In methods such as HMC, the variables $\boldsymbol{\theta}$ and $\boldsymbol{p}$ are treated as independent and therefore their joint probability distribution can be expressed as (e.g., Betancourt, 2018):

$$\Pi(\boldsymbol{\theta}, \boldsymbol{p}) = \Pi'(\boldsymbol{\theta})\, \Pi(\boldsymbol{p}) \tag{B1}$$

where $\Pi'(\boldsymbol{\theta})$ is the total probability of observing $\boldsymbol{\theta}$ and $\Pi(\boldsymbol{p})$ is the total probability of observing $\boldsymbol{p}$. In the literature, $\Pi'(\boldsymbol{\theta})$ is often referred to as the target probability. Equation (B1) shows that the total probability of a system with $\boldsymbol{\theta}$ and $\boldsymbol{p}$ can be calculated if we multiply the independent probabilities of $\boldsymbol{\theta}$ and $\boldsymbol{p}$. In the statistical application of HMC, we require some formulation that connects this joint probability of the variables with the Hamiltonian energy. This is done by borrowing concepts from statistical mechanics and expressing the joint probability as:

$$\Pi(\boldsymbol{\theta}, \boldsymbol{p}) \propto \exp[-H(\boldsymbol{\theta}, \boldsymbol{p})] \tag{B2}$$

Equation (B2) represents a Boltzmann distribution which shows that the total probability of a state $\Pi(\boldsymbol{\theta}, \boldsymbol{p})$, that is described by $\boldsymbol{\theta}$ and $\boldsymbol{p}$, is proportional to the Hamiltonian energy. Equation (B2) expresses the fact that configurations with lower (Hamiltonian) energies are more probable to occur. Replacing $H(\boldsymbol{\theta}, \boldsymbol{p})$ from Equation (1) in the main text into Equation (B2) results to:

$$\Pi(\boldsymbol{\theta}, \boldsymbol{p}) \propto \exp[-H(\boldsymbol{\theta}, \boldsymbol{p})] = \exp[-V(\boldsymbol{\theta})]\, \exp[-T(\boldsymbol{p})] \tag{B3}$$

Direct comparison between Equations (B1) and (B3) reveals the following relation:

$$\Pi'(\boldsymbol{\theta})\, \Pi(\boldsymbol{p}) \propto \exp[-V(\boldsymbol{\theta})]\, \exp[-T(\boldsymbol{p})]$$

which in turn shows that:

$$\Pi'(\boldsymbol{\theta}) \propto \exp[-V(\boldsymbol{\theta})]$$
$$\Pi(\boldsymbol{p}) \propto \exp[-T(\boldsymbol{p})] \tag{B4}$$

Equation (B4) describes the independent probability distributions of $\boldsymbol{\theta}$ and $\boldsymbol{p}$ as Boltzmann distributions. Then, in Bayesian HMC approaches, the potential energy is chosen in the following way (e.g., Neal, 2011):

$$V(\boldsymbol{\theta}) = -\log\big[\Pi(\boldsymbol{\theta} \mid F^{\text{obs}})\big] \tag{B5}$$

where $\Pi(\boldsymbol{\theta} \mid F^{\text{obs}})$ is the conditional probability of observing the parameters $\boldsymbol{\theta}$ given that we know the observed data F^{obs} and log represents the natural logarithm. $\Pi(\boldsymbol{\theta} \mid F^{\text{obs}})$ is also referred to as the posterior probability in the literature. Due to this particular choice of potential energy, we can substitute Equation (B5) in Equation (B4) and observe that:

$$\Pi'(\boldsymbol{\theta}) \propto \Pi(\boldsymbol{\theta} \mid F^{\text{obs}}) \tag{B6}$$

Therefore, this exact choice of potential energy makes the target distribution directly related to the posterior distribution without explicit normalization factors. The posterior probability can be further calculated with Bayes' theorem. If we neglect the effect of the marginal probability of observing F^{obs} (e.g., Bailer-Jones, 2017, p. 64), then the unnormalized posterior probability can be written in the following way:

$$\Pi(\boldsymbol{\theta} \mid F^{\text{obs}}) = L(F^{\text{obs}} \mid \boldsymbol{\theta})\,\Pi(\boldsymbol{\theta}) \tag{B7}$$

where $L(F^{\text{obs}} \mid \boldsymbol{\theta})$ is the likelihood and $\Pi(\boldsymbol{\theta})$ is the prior distribution (see main text). Now it is possible to substitute Equation (B7) into Equation (B5):

$$V(\boldsymbol{\theta}) = -\log\big[L(F^{\text{obs}} \mid \boldsymbol{\theta})\,\Pi(\boldsymbol{\theta})\big] \tag{B8}$$

For kinetic energy, the same definition is used as in Equation (5) of the main text. By substituting Equation (5) from the main text into Equation (B4) we see that:

$$\Pi(\boldsymbol{p}) \propto \exp\big(-\tfrac{1}{2}\,\boldsymbol{p}^{\mathrm{T}}\mathbf{M}^{-1}\boldsymbol{p}\big) \tag{B9}$$

Equation (B9) shows that the momenta $\boldsymbol{p}$ are simply described by a Gaussian distribution. This distribution is easily sampled from and has well-known analytical derivatives which help the efficiency of the algorithm. Finally, if the kinetic and potential energy are substituted into the Hamiltonian energy (Eq. 1 in the main text), we end up with the equation that most Bayesian HMC approaches use:

$$H(\boldsymbol{\theta}, \boldsymbol{p}) = \tfrac{1}{2}\,\boldsymbol{p}^{\mathrm{T}}\mathbf{M}^{-1}\boldsymbol{p} - \log\big[L(F^{\text{obs}} \mid \boldsymbol{\theta})\,\Pi(\boldsymbol{\theta})\big] \tag{B10}$$

C The HMC algorithm in five steps

The following section is presenting the standard HMC algorithm shown in Betancourt (2018) and Neal (2011) but offers additional clarity for readers interested in the application of HMC.
Step 1: During the initial step, a sample $\boldsymbol{\theta}_{\text{current}}$ (the invertible parameters in the main text) is drawn based on the prior distribution $\Pi(\boldsymbol{\theta})$. The prior distribution represents prior beliefs about the parameter based on existing knowledge. In the absence of such knowledge, a more diffused or non-informative prior is typically chosen to represent greater uncertainty.
Step 2: A sample for $\boldsymbol{p}_{\text{current}}$ is randomly drawn from a normal distribution $\mathcal{N}(\mathbf{0}, \mathbf{M})$ where $\mathbf{0}$ denotes the mean value and $\mathbf{M}$ represents the variance or covariance matrix of momenta.
Step 3: Based on $\boldsymbol{\theta}_{\text{current}}$ and $\boldsymbol{p}_{\text{current}}$, the Hamiltonian dynamics are simulated by numerically solving the canonical equations (Eq. 7 & 8 of the main text) for n_t steps and a step size of Δt. This step of the algorithm is deterministic. However, all numerical discretization methods that solve the canonical equations introduce some degree of error, which can result in either an artificial gain or loss of Hamiltonian energy over time (e.g., Fichtner et al., 2021; their Appendix C). Among the various explicit numerical algorithms, the leapfrog algorithm has been proven to be

particularly effective and widely used for solving the Hamiltonian equations (Mikkola & Tanikawa, 1999; Yoshida, 1990). A key consideration in implementing the leapfrog method is the careful selection of n_t and Δt. These parameters must be chosen in such a way to ensure both the efficient exploration of the Hamiltonian trajectory and the stability of the numerical integration scheme (Betancourt et al., 2015; Fichtner et al., 2021; Neal, 2011). After simulating a Hamiltonian trajectory for n_t steps, the system makes a large jump using the gradient information and reaches a new state characterized by $\boldsymbol{\theta}_{\text{new}}$ and $\boldsymbol{p}_{\text{new}}$.

Step 4: The next part of the algorithm determines if the new state will be accepted or not. It is common that, after simulating a single trajectory of Hamiltonian dynamics, the numerical integration leads to a Hamiltonian value different from the initial one. As a result, the joint total probability may change not because of physical reasons but because of the numerical implementation. This can introduce bias in the sampling. Therefore, a correction mechanism is required to prevent this bias. First, the new vector of momenta is negated from $\boldsymbol{p}_{\text{new}}$ to $-\boldsymbol{p}_{\text{new}}$. Then, the Hamiltonian energy for the current step $H(\boldsymbol{\theta}_{\text{current}}, \boldsymbol{p}_{\text{current}})$ and the new step $H(\boldsymbol{\theta}_{\text{new}}, -\boldsymbol{p}_{\text{new}})$ are computed. Then the new state is accepted with probability:

$$\alpha = \min(1, \exp[H(\boldsymbol{\theta}_{\text{current}}, \boldsymbol{p}_{\text{current}}) - H(\boldsymbol{\theta}_{\text{new}}, -\boldsymbol{p}_{\text{new}})]) \tag{C1}$$

Equation (C1) is also referred to as the Metropolis criterion. It constitutes a simplification of the Metropolis–Hastings criterion (Hastings, 1970; Metropolis et al., 1953). If the Hamiltonian energy remains exactly conserved during numerical integration, then the exponential term of Equation (C1) equals 1 and the new state is accepted with probability 1 (i.e., 100%). If the numerical implementation introduces errors such that $H(\boldsymbol{\theta}_{\text{new}}, -\boldsymbol{p}_{\text{new}}) > H(\boldsymbol{\theta}_{\text{current}}, \boldsymbol{p}_{\text{current}})$, this implies a violation of energy conservation. In this case, the exponential term becomes less than 1 and the new state is accepted with probability less than 1. During this step, it is crucial to negate the momentum vector. The negation is permitted due to the reversibility of Hamiltonian dynamics but is also essential. Without it, the Metropolis acceptance criterion would always evaluate to zero and no sample updates could be accepted (see Betancourt, 2018; section 5.2).

It is also important to note that the Hamiltonian dynamics are volume-preserving (Liouville's theorem). This means that any region R in phase space will preserve its volume after a transformation due to Hamiltonian dynamics, which is equal to the preservation of the total probability distribution. If this was not the case, a Metropolis–Hastings criterion would be required instead. The Metropolis–Hastings criterion considers the effect of volume transformations of the phase space that can effectively change the probability distributions. In a non-volume-preserving scenario the determinant of the Jacobian matrix of the mapping between the current and new state would be required to track how the probability densities change due to the transformation of the phase space (e.g., Eidsvik & Tjelmeland, 2006).

Step 5: If the proposed state is rejected, the sampler retains the current position $\boldsymbol{\theta}_{\text{current}}$ and a new momentum is randomly drawn from the Gaussian distribution $\mathcal{N}(\mathbf{0}, \mathbf{M})$. If the proposed state is accepted, the sampler proceeds from $\boldsymbol{\theta}_{\text{new}}$. During the next iteration, a new momentum $\boldsymbol{p}'_{\text{new}}$ from a normal distribution $\mathcal{N}(\mathbf{0}, \mathbf{M})$ is sampled. Steps (2) through (5) are then repeated, allowing the algorithm to make large jumps in the typical set and efficiently explore it. The random choice of momenta in HMC corresponds to the stochastic nature of the algorithm.

The large parameter jumps, driven by the canonical equations in Step 3, help HMC escape local minima and reach unexplored areas of the typical set quickly. Furthermore, the formulation of the kinetic energy, which is inspired by physical systems, ensures conservation of Hamiltonian energy and non-dissipative behaviour towards the mode. Finally, stochastic (random) transitions between different Hamiltonian energy level sets enable the sampler to explore a broader range of acceptable fit magnitudes while avoiding the mode but also areas of bad fits.

D GDIFF

GDIFF (Moulas, 2023) is a Finite Difference (FD) numerical code used to calculate the concentration profiles of garnet in one dimension. In multicomponent diffusion, the concentration profile of each endmember depends on the composition gradients of the other endmembers. This

behavior is described by the multicomponent diffusion equation:

$$\frac{\partial C_i}{\partial t} = \frac{1}{x^{n-1}} \frac{\partial}{\partial x} \left(x^{n-1} D_{ij} \frac{\partial C_j}{\partial x} \right) \tag{D1}$$

where x is the spatial coordinate, t is time, C is the mole fraction concentration, i and j are indices representing the independent endmembers, n is an integer that can be used to specify the geometry of the mineral and D_{ij} is the diffusivity matrix that accounts for the coupling between them. The diffusivity matrix is composition-dependent and is calculated following the approach of Lasaga (1979):

$$D_{ij} = D_i^* \delta_{ij} - \frac{D_i^* X_i}{\sum_{k=1}^{4} D_k^* X_k} (D_j^* - D_4^*) \tag{D2}$$

where D_i^* is the tracer-diffusion coefficient of each endmember, δ_{ij} is the Kronecker delta, and X_i represents the mole fractions of each endmember. Tracer diffusivity coefficients are taken from Chakraborty & Ganguly (1992) and follow an Arrhenius relationship, making them temperature- and pressure-dependent.

Equation (D1) is solved on a regularly spaced grid using an implicit, conservative scheme. Because diffusivities depend on composition and vary with space, Picard iterations are used to achieve numerical convergence, with a tolerance threshold of 10^{-5}. This makes the problem non-linear. The equations are discretized and written in a matrix-vector form as:

$$\mathbf{A}\,\mathbf{x}^{m} = \mathbf{b} \tag{D3}$$

In this form, $\mathbf{A}$ contains the coefficients of the unknowns, $\mathbf{x}$ is the vector of unknown concentrations, m is the Picard iteration number, and $\mathbf{b}$ is the right-hand side vector built from the previous physical timestep. For more details refer to Moulas (2023).

E KADMOS

KADMOS (Moulas & Brandon, 2022) is a Finite Element (FE) numerical code used to model the apparent (^{40}K/^{40}Ar) ages and the associated (^{40}Ar/^{39}Ar) ages of different minerals for a given P-T-t path. KADMOS is solving the diffusion equation with a source term to account for the production of radiogenic ^{40}Ar. The main equation that is solved is:

$$x^{n-1} \frac{\partial}{\partial t} \left(\frac{\mathrm{Ar}}{K_0} \right) = \frac{\partial}{\partial x} \left[x^{n-1} D \frac{\partial}{\partial x} \left(\frac{\mathrm{Ar}}{K_0} \right) \right] + x^{n-1} \lambda_{\mathrm{Ar}} e^{-\lambda_T t} \tag{E1}$$

where x represents the spatial coordinate, n is an integer specifying the geometry of the mineral, Ar represents the radiogenic argon produced from the decay of potassium, K_0 is the initial amount of ^{40}K, D is the diffusion coefficient that is independent of concentration, λ_{Ar} is the decay constant of ^{40}K to ^{40}Ar ($0.581 \cdot 10^{-10}\,\mathrm{yrs}^{-1}$), λ_T is the total decay constant of ^{40}K ($5.543 \cdot 10^{-10}\,\mathrm{yrs}^{-1}$) and t is time. The second term of the right-hand side of Eq. (E1) corresponds to the accumulation of radiogenic argon with time while the rest of the equation is responsible for the diffusion of argon in the mineral with time. Therefore, the simulations of KADMOS start from the formation of the mineral at $t = 0$ until a total time with a P-T-t path that can be specified by the user.

For the discretization of Equation (E1) a Galerkin approach is used. Also, linear shape functions in a global coordinate scope are adopted. The discretized form of Equation (E1) is as follows:

$$\mathbf{KM}\,\{C_i^j\} = \mathbf{R} \tag{E2}$$

where $\mathbf{KM}$ is the global left-hand side matrix, $\mathbf{R}$ is the global right-hand side vector, and C_i^j represents the unknowns (degrees of freedom) at point i and time j. The global matrices are assembled by combining the local matrices that correspond to each element. KADMOS assumes that ^{40}Ar leaves at the outer boundary of a crystal. This imposes a large compositional gradient that might lead to numerical instability. To overcome this problem, KADMOS utilizes an adaptive grid that resolves large gradients in detail. For a detailed description of the numerical implementation and theory refer to Moulas & Brandon (2022).

SUPPLEMENTARY FIGURES FOR

Hamiltonian Monte Carlo applied to inverse petrological problems

Dimitrios Moutzouris[1], Annalena Stroh[1], Simon Schorn[1], Evangelos Moulas[1]

[1]Institute of Geosciences and Mainz Institute of Multiscale Modeling (M[3]ODEL), Johannes-Gutenberg University, Mainz, Germany

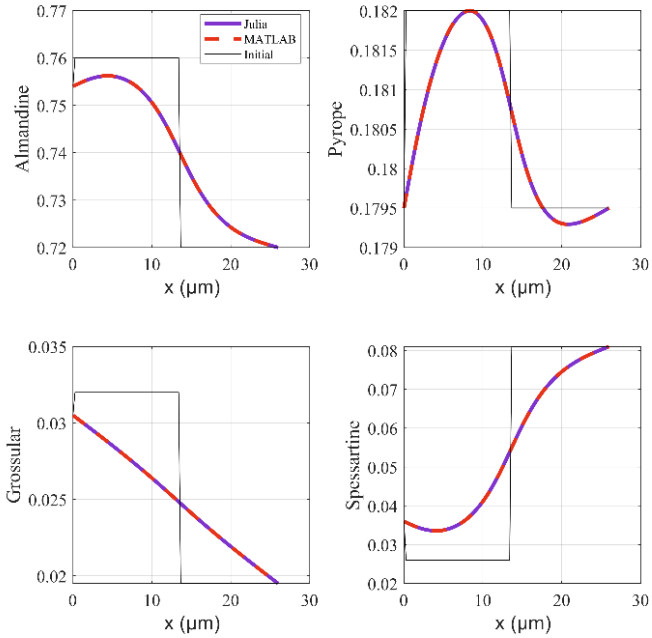

Figure S1. Compositional profiles of garnet demonstrating agreement between the MATLAB and Julia implementation of GDIFF. The same numerical and physical parameters have been used.

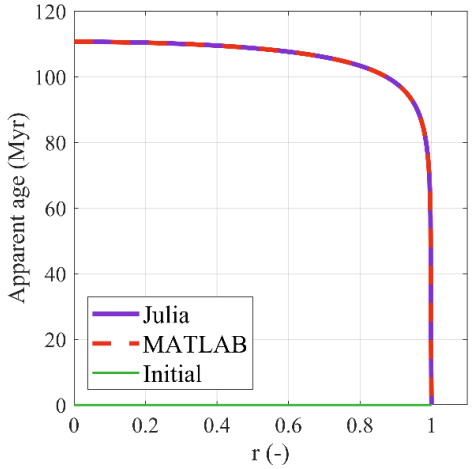

Figure S2. Apparent age profile demonstrating agreement between the MATLAB and Julia implementation of KADMOS. The same numerical and physical parameters have been used.

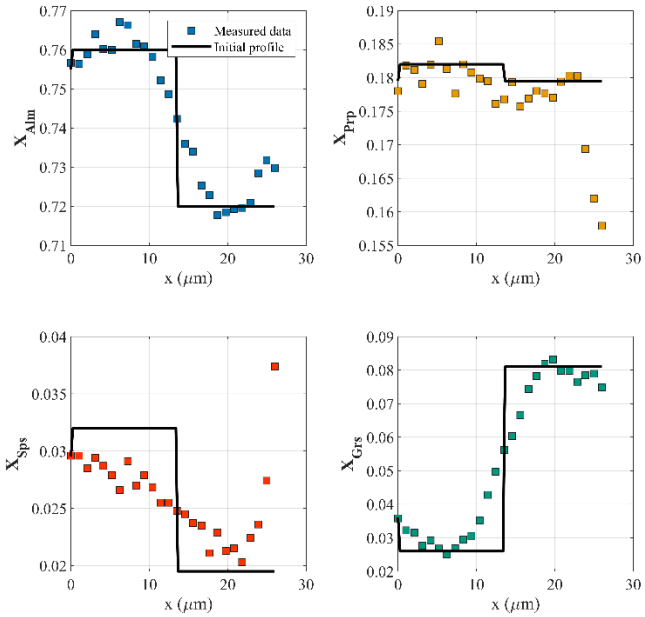

Figure S3. Measured compositional profiles of Grt7 (squares) and initial conditions (black lines) used for the evaluation of GDIFF models.

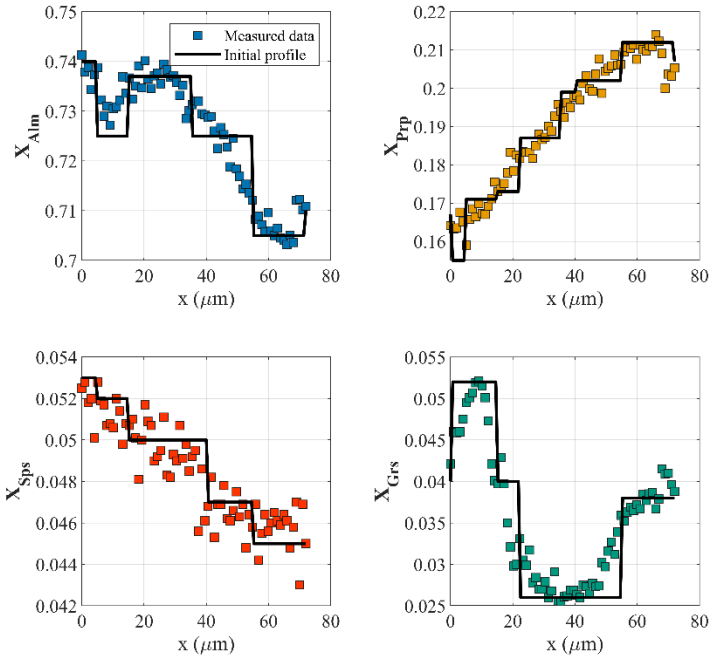

Figure S4. Measured compositional profiles of Grt15 (squares) and initial conditions (black lines) used for the evaluation of GDIFF models.

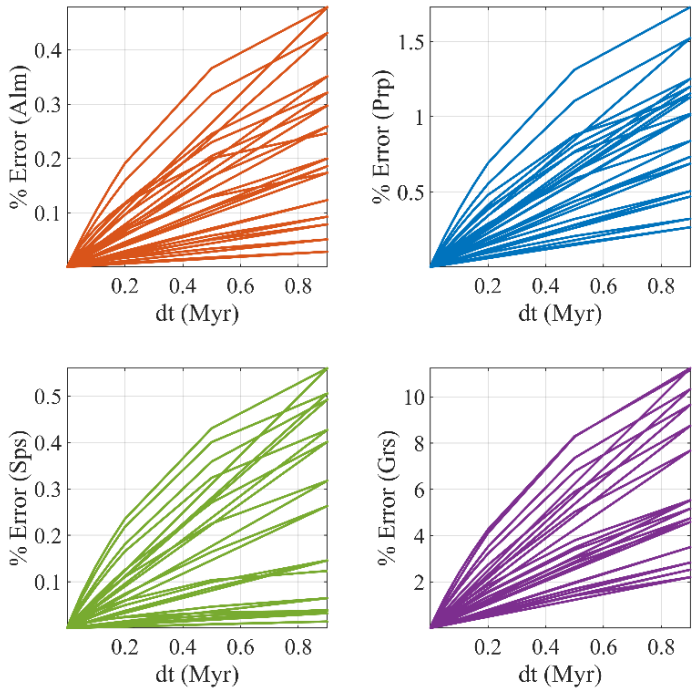

Figure S5. Plots showing the percentage of error generated for each modeled endmember of garnet with GDIFF for different numerical timesteps (dt). Different cooling rates and initial temperatures were tested spanning the investigated range. A timestep of 0.02 Myr was chosen as it produces errors well-below 1%.

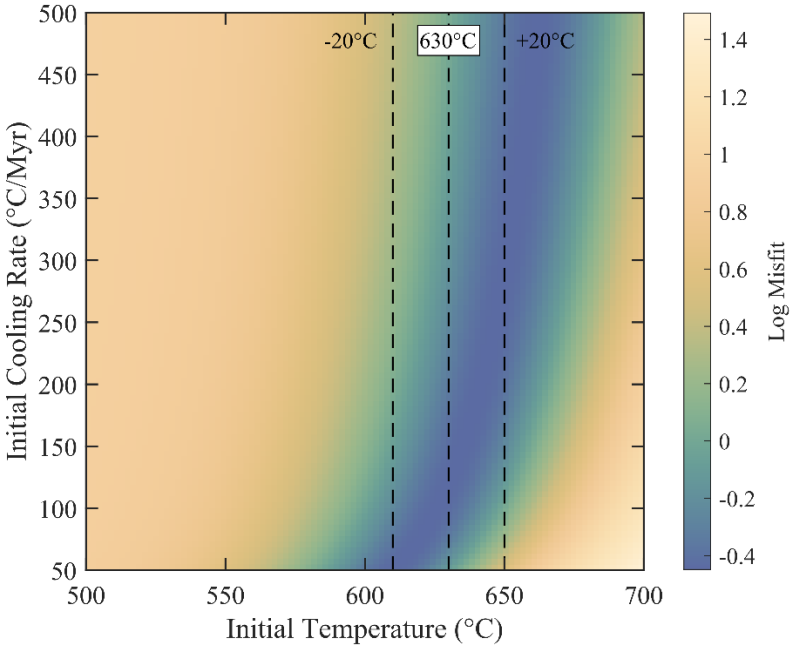

Figure S6. Misfit map for all considered combinations of initial temperature and initial cooling rate using GDIFF. The misfit quantifies the difference between modeled and measured garnet compositions. This misfit map was constructed by assuming that the grossular component is ten times more important than the other three components.

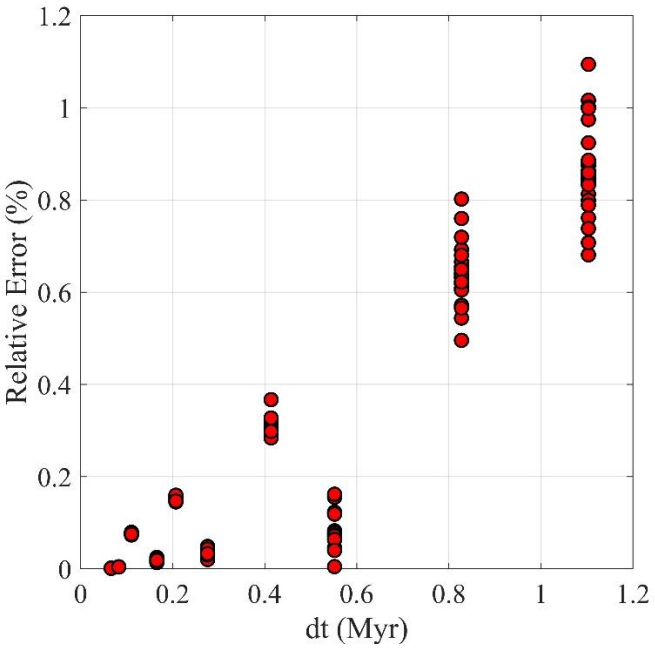

Figure S7. Plot representing the relative percentage of error generated using different timesteps in KADMOS. Different cooling rates and initial temperatures were tested spanning the entire investigated range. A timestep of 0.27 Myr was chosen as it produces errors well-below 1%.

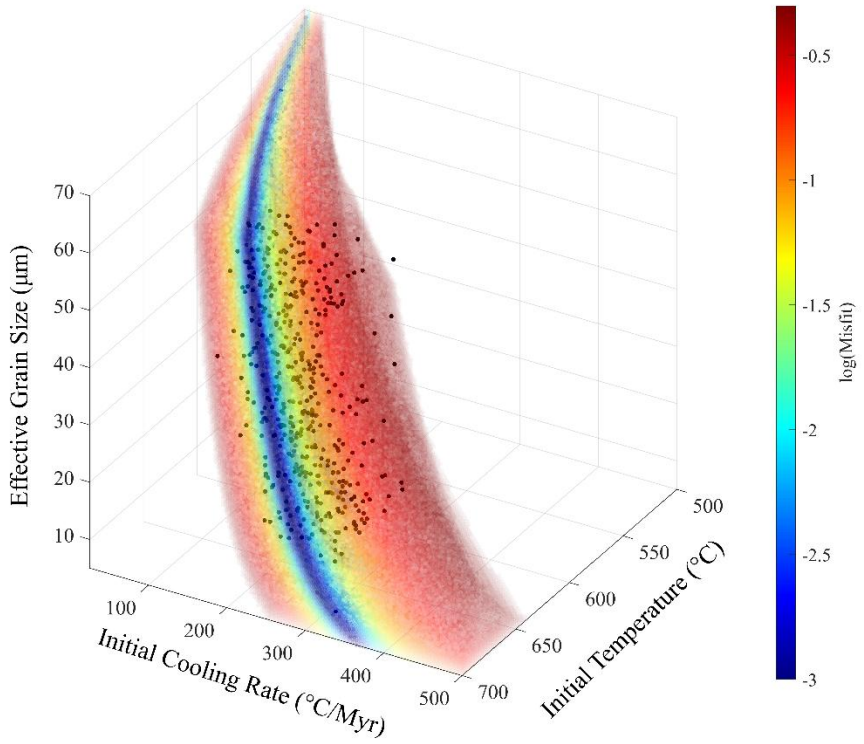

Figure S8. Direct search results for a three-dimensional case using KADMOS. The misfit quantifies the difference between modeled and measured muscovite age. Misfits with values lower than 0.6 Myr are plotted here. The black dots represent the samples drawn from HMC (see main text for more details). A clear zone of low misfits is indicated showing how the effective grain size has not a significant effect on the measured age.

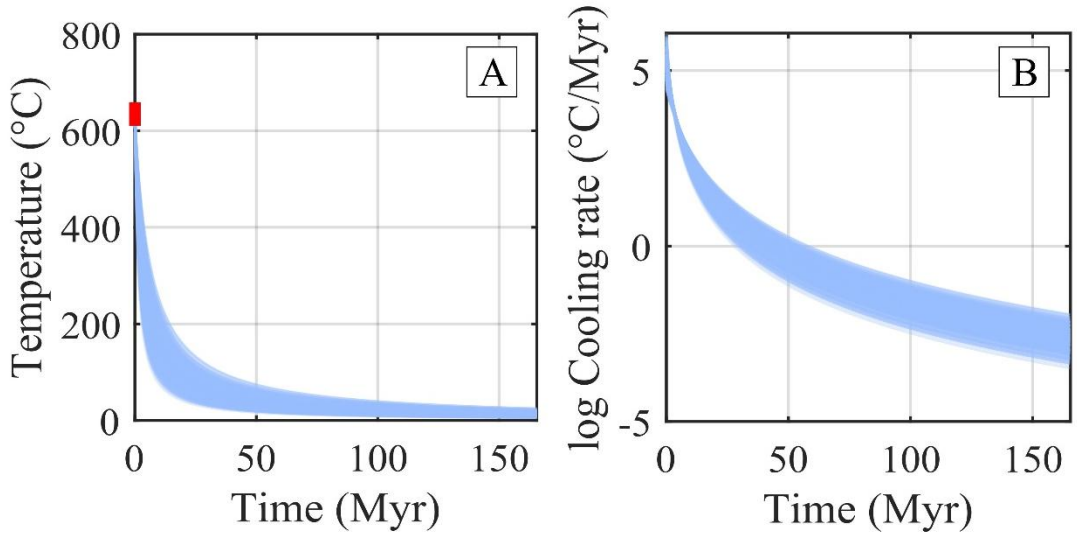

Figure S9. (A) Time-temperature diagram illustrating the cooling paths corresponding to the accepted initial cooling rates and initial temperatures derived from the HMC analysis. The thick red band denotes the range of accepted initial equilibration temperatures. (B) Cooling rate evolution for each of the accepted cooling paths